

Evidence for Interhemispheric Mercury Exchange in the Pacific Ocean Upper Troposphere

Alkuin M. Koenig, Jeroen E. Sonke, Olivier Magand, Marcos Andrade, Isabel Moreno, Fernando Velarde, Ricardo Forno, René Gutierrez, Luis Blacutt, Paolo Laj, et al.

▶ **To cite this version:**

Alkuin M. Koenig, Jeroen E. Sonke, Olivier Magand, Marcos Andrade, Isabel Moreno, et al.. Evidence for Interhemispheric Mercury Exchange in the Pacific Ocean Upper Troposphere. Journal of Geophysical Research: Atmospheres, 2022, 127, 10.1029/2021JD036283 . insu-03706371

HAL Id: insu-03706371
https://insu.hal.science/insu-03706371

Submitted on 28 Jun 2022

HAL is a multi-disciplinary open access archive for the deposit and dissemination of scientific research documents, whether they are published or not. The documents may come from teaching and research institutions in France or abroad, or from public or private research centers.

L'archive ouverte pluridisciplinaire **HAL**, est destinée au dépôt et à la diffusion de documents scientifiques de niveau recherche, publiés ou non, émanant des établissements d'enseignement et de recherche français ou étrangers, des laboratoires publics ou privés.



Distributed under a Creative Commons Attribution 4.0 International License

Check for updates

JGR Atmospheres

RESEARCH ARTICLE
10.1029/2021JD036283

Evidence for Interhemispheric Mercury Exchange in the Pacific Ocean Upper Troposphere

Alkuin M. Koenig[1], Jeroen E. Sonke[2], Olivier Magand[1], Marcos Andrade[3,4], Isabel Moreno[3], Fernando Velarde[3], Ricardo Forno[3], René Gutierrez[3], Luis Blacutt[3], Paolo Laj[1], Patrick Ginot[1], Johannes Bieser[5], Andreas Zahn[6], Franz Slemr[7], and Aurélien Dommergue[1]

[1]Institut des Géosciences de l'Environnement, CNRS, IRD, Grenoble INP, Université Grenoble Alpes, Grenoble, France, [2]Géosciences Environnement Toulouse, CNRS/IRD/Université Paul Sabatier Toulouse 3, Toulouse, France, [3]Laboratorio de Física de la Atmósfera (LFA), Instituto de Investigaciones Físicas, Universidad Mayor de San Andrés, La Paz, Bolivia, [4]Department of Atmospheric and Oceanic Science, University of Maryland, College Park, MD, USA, [5]Helmholtz-Zentrum Hereon, Institute of Coastal Research, Geesthacht, Germany, [6]Karlsruhe Institute of Technology, Institute of Meteorology and Climate Research, Karlsruhe, Germany, [7]Max Planck Institute for Chemistry, Mainz, Germany

Key Points:

- We use the strong increase in atmospheric Hg at Chacaltaya mountain in tropical South America during the 2015–2016 El Niño for a case study
- In 2015–2016, air mass origin for Chacaltaya shifted westward, with greatly enhanced influence of the tropical Pacific upper troposphere (UT)
- Our results suggest that interhemispheric exchange in the tropical Pacific UT can bring Northern Hemisphere Hg to Chacaltaya

Supporting Information:

Supporting Information may be found in the online version of this article.

Correspondence to:

A. M. Koenig,
alkuin-maximilian.koenig@univ-grenoble-alpes.fr

Citation:

Koenig, A. M., Sonke, J. E., Magand, O., Andrade, M., Moreno, I., Velarde, F., et al. (2022). Evidence for interhemispheric mercury exchange in the Pacific Ocean upper troposphere. *Journal of Geophysical Research: Atmospheres*, *127*, e2021JD036283. https://doi.org/10.1029/2021JD036283

Received 29 NOV 2021
Accepted 8 MAY 2022

Author Contributions:

Conceptualization: Alkuin M. Koenig, Jeroen E. Sonke, Olivier Magand, Johannes Bieser, Aurélien Dommergue
Data curation: Olivier Magand, Marcos Andrade, Isabel Moreno, Fernando Velarde, René Gutierrez, Andreas Zahn
Formal analysis: Alkuin M. Koenig, Franz Slemr

© 2022. The Authors.
This is an open access article under the terms of the Creative Commons Attribution License, which permits use, distribution and reproduction in any medium, provided the original work is properly cited.

Abstract Even though anthropogenic mercury (Hg) emissions to the atmosphere are ~2.5 times higher in the Northern Hemisphere (NH) than in the Southern Hemisphere (SH), atmospheric Hg concentrations in the NH are only ~1.5 times higher than in the SH. Global Hg models attribute this apparent discrepancy to large SH oceanic Hg emissions or to interhemispheric exchange of Hg through the atmosphere. However, no observational data set exists to serve as a benchmark to validate whether these coarse-resolution models adequately represent the complex dynamics of interhemispheric Hg exchange. During the 2015–2016 El Niño, we observed at mount Chacaltaya in the tropical Andes a ~50% increase in ambient Hg compared to the year before, coinciding with a shift in synoptic transport pathways. Using this event as a case study, we investigate the impact of interhemispheric exchange on atmospheric Hg in tropical South America. We use HYSPLIT to link Hg observations to long-range transport and find that the observed Hg increase relates strongly to air masses from the tropical Pacific upper troposphere (UT), a region directly impacted by interhemispheric exchange. Inclusion of the modeled seasonality of interhemispheric air mass exchange strengthens this relationship significantly. We estimate that interhemispheric exchange drives Hg seasonality in the SH tropical Pacific UT, with strongly enhanced Hg between July and October. We validate this seasonality with previously published aircraft Hg observations. Our results suggest that the transport of NH-influenced air masses to tropical South America via the Pacific UT occurs regularly but became more detectable at Chacaltaya in 2015–2016 because of a westward shift in air mass origin.

Plain Language Summary Human activities have released much more mercury, a toxic pollutant, into the Northern Hemisphere (NH) atmosphere than into the Southern Hemisphere (SH) atmosphere. Yet, the difference in mercury concentrations between the two hemispheres is not very large. Model studies attribute this unexpectedly low interhemispheric mercury difference to large emissions from SH oceans or to the exchange of airborne mercury between hemispheres. This interhemispheric mercury exchange is complex, however, and direct observational evidence is lacking. Here, we examine the strong increase in atmospheric mercury during the 2015–2016 El Niño at mount Chacaltaya in tropical South America. We examine and exclude potential SH sources for this increase, such as mercury emissions from wildfires or marine mercury emissions. Instead, we find that this mercury increase was likely caused by interhemispheric mercury exchange at high altitudes over the tropical Pacific Ocean, and the subsequent transport of mercury-rich NH-influenced air to tropical South America. We propose that Chacaltaya mercury observations could be used as a reference to test if current mathematical models can correctly predict interhemispheric mercury exchange.

1. Introduction

Mercury (Hg) is toxic and bioaccumulates in aquatic food chains. Due to its long atmospheric lifetime, Hg released into the atmosphere is transported to places far from its point of emission. Marine Hg re-emission (mostly legacy) appears to be the largest atmospheric Hg source (~4,600 Mg yr^{-1}), followed by primary anthropogenic (~2,300 Mg yr^{-1}) and terrestrial emissions (~1,300 Mg yr^{-1}; Horowitz et al., 2017). Modern anthropogenic

Funding acquisition: Marcos Andrade, Ricardo Forno, Paolo Laj, Patrick Ginot, Aurélien Dommergue
Investigation: Olivier Magand, Isabel Moreno, Fernando Velarde, René Gutierrez, Patrick Ginot, Andreas Zahn, Franz Slemr, Aurélien Dommergue
Methodology: Alkuin M. Koenig, Johannes Bieser
Project Administration: Jeroen E. Sonke, Paolo Laj, Aurélien Dommergue
Resources: Marcos Andrade, Ricardo Forno, Luis Blacutt, Andreas Zahn, Franz Slemr, Aurélien Dommergue
Software: Alkuin M. Koenig
Supervision: Jeroen E. Sonke, Marcos Andrade, Ricardo Forno, Aurélien Dommergue
Validation: Alkuin M. Koenig, Olivier Magand, Franz Slemr
Visualization: Alkuin M. Koenig
Writing – original draft: Alkuin M. Koenig, Jeroen E. Sonke, Olivier Magand, Aurélien Dommergue
Writing – review & editing: Alkuin M. Koenig, Jeroen E. Sonke, Olivier Magand, Marcos Andrade, Isabel Moreno, Fernando Velarde, Luis Blacutt, Paolo Laj, Johannes Bieser, Franz Slemr, Aurélien Dommergue

Hg emissions to the atmosphere are 5–10 times larger than natural volcanic and soil degassing emissions (C. Li et al., 2020; UN-Environment, 2019). Since the industrial revolution, human activities have released over 3 times more mercury into the Northern Hemisphere (NH) atmosphere than into the Southern Hemisphere (SH) atmosphere (Streets et al., 2017). Modern anthropogenic Hg emissions to the atmosphere are still ∼2.5 times higher in the NH than in the SH (Streets et al., 2017; UN-Environment, 2019), with about half of the global total being emitted in Asia (Song et al., 2015; Streets et al., 2017). Despite these large hemispheric differences in direct anthropogenic emissions, Hg concentrations at surface monitoring stations are only ∼1.5 times higher in the NH than in the SH, with mean Hg^0 of 1.3–1.6 ng/m^3 in the NH, 1.1–1.3 ng/m^3 in the tropics, and 0.8–1.1 ng/m^3 in the SH (Obrist et al., 2018; Sprovieri et al., 2016).

While some model studies attributed this unexpectedly low interhemispheric Hg gradient to interhemispheric exchange (Shah et al., 2021), others argued that it mainly results from the large magnitude of SH oceanic Hg emissions (Horowitz et al., 2017). Previous studies used the surface-level interhemispheric Hg gradient to constrain interhemispheric Hg exchange and Hg lifetime (Lamborg et al., 2002; Selin et al., 2007; Travnikov et al., 2017). In a two-hemisphere box model approach, Lamborg et al. (2002) used the interhemispheric gradient and the mean interhemispheric air mass exchange time to estimate net interhemispheric NH to SH Hg exchange. The mean interhemispheric air mass exchange time is around 1.3 yr (Czeplak & Junge, 1975; Geller et al., 1997; Patra et al., 2009), which implies that within a year ∼1/1.3 (∼77%) of tropospheric NH air mass enters the SH and vice versa (Czeplak & Junge, 1975). This yields a net Hg input of ∼800 Mg yr^1 into the SH due to interhemispheric exchange, which is about as much as SH anthropogenic emissions (∼650 Mg yr^1; Streets et al., 2017) and SH biomass burning (BB) emissions combined (BB globally: ∼220–300 Mg yr^{-1}; Horowitz et al., 2017; Shah et al., 2021). However, Horowitz et al. (2017) argued that due to the potentially large SH marine Hg emissions, the interhemispheric Hg gradient cannot be directly used to constrain atmospheric Hg lifetime and interhemispheric Hg exchange.

Studies have also shown that interhemispheric air mass exchange is not constant but varies both spatially and temporally: The interhemispheric exchange of long-lived pollutants such as CFCs and CO_2 predominantly occurs in the tropical upper troposphere (UT; Orbe et al., 2016; Prather et al., 1987). Interhemispheric air mass exchange exhibits a seasonality driven by seasonal displacements of the Hadley cell (Bowman & Cohen, 1997; Miyazaki et al., 2009), monsoonal circulations (G. Chen et al., 2017; Yan et al., 2021), and Rossby wave propagation (Francey & Frederiksen, 2016; Frederiksen & Francey, 2018; Y. Li et al., 2015). Interhemispheric air mass exchange is also not zonally symmetric but is for instance enhanced close to monsoon systems, especially the Asian summer monsoon (Yan et al., 2021).

If the atmospheric lifetime of a compound is significantly shorter than the mean interhemispheric exchange time of ∼1.3 yr, then the compound's interhemispheric exchange increasingly depends on the temporal and spatial distribution of its sources and sinks within each hemisphere. This becomes important for lifetimes below ∼6 months (Aghedo et al., 2010; Czeplak & Junge, 1975) and may apply to atmospheric Hg: estimates for the average lifetime of elemental Hg^0, the most prominent Hg species in the atmosphere, range from 1.7 yr down to 5.2 months (Ariya et al., 2015; Gonzalez-Raymat et al., 2017; Horowitz et al., 2017; Shah et al., 2021). Uncertainties in Hg redox chemistry and Hg oxidant concentrations are significant, and important Hg redox mechanisms might still be missing (Saiz-Lopez et al., 2020). The inclusion of such new redox schemes can alter modeled atmospheric Hg lifetime considerably (Horowitz et al., 2017; Saiz-Lopez et al., 2018, 2020; Shah et al., 2021).

Considering the uncertainties in Hg lifetime and the complexity of interhemispheric exchange, it is unclear whether global Eulerian chemical transport models in their frequently used low-resolution setup (∼5° longitude x 4° latitude, 47–72 vertical levels) can adequately represent interhemispheric Hg exchange. These models tend to underestimate vertical transport (Yu et al., 2018), and numerically dissolve plumes and narrow transport channels (Eastham & Jacob, 2017; Zhuang et al., 2018).

We know of no suitable observational data set to validate model results with respect to interhemispheric Hg exchange. While important evidence for low-altitude interhemispheric Hg exchange comes from the Australian Tropical Atmospheric Research Station (ATARS), where elevated Hg was detected in air masses episodically originating from the NH (Howard et al., 2017), this data set cannot capture the dominant UT pathway (Orbe et al., 2016; Prather et al., 1987) of interhemispheric exchange. UT Hg observations in the NH and SH are provided by CARIBIC flights ("Civil Aircraft for the Regular Investigation of the Atmosphere Based on an

Instrument Container"; Slemr et al., 2009), but CARIBIC data lacks spatial and temporal continuity. Recently, we presented a new data set that could be highly relevant to study interhemispheric Hg exchange. During the exceptionally strong 2015–2016 El Niño, a strong and yet unexplained rise in total gaseous mercury (TGM) was detected at mount Chacaltaya (CHC, 5,240 m asl.) in the tropical Bolivian Andes in South America, where TGM was measured continuously for 20 months. In 2015, TGM concentrations at CHC rose within less than 6 months from typical SH levels (∼0.9 ng/m^3) to values comparable to the NH background (∼1.5 ng/m^3; Koenig et al., 2021; Figure 2a).

A link between atmospheric Hg and El Niño appears plausible, given the widespread effects of El-Niño-Southern-Oscillation (ENSO). ENSO is a coupled ocean-atmosphere phenomenon that affects moisture flux and transport pathways by directly impacting the meridional-vertical Hadley cell and the zonal-vertical Walker circulation (Ambrizzi et al., 2004; Grimm & Ambrizzi, 2009). El Niño conditions are often associated with an eastward shift of the Pacific Walker circulation. Such a shift enhances convection over the central equatorial Pacific and tends to suppress convection over tropical South America, favoring the subsidence of westerly air masses from the Pacific sector (Ambrizzi et al., 2004; Grimm & Ambrizzi, 2009; Lau & Yang, 2015). ENSO can alter ocean re-emissions (Chatterjee et al., 2017; Huang & Zhang, 2021), BB emissions (Y. Chen et al., 2011; Liu et al., 2017), and gas exchange by vegetation (Bastos et al., 2018; Koren et al., 2018; Liu et al., 2017). However, while previous studies have suggested that ENSO could impact tropospheric Hg concentrations (Franz Slemr et al., 2016), the magnitude of the CHC TGM increase during the 2015–2016 El Niño is unprecedented.

Here, we explore the strong increase in CHC TGM in 2015. First, we evaluate if changes in BB Hg emissions, vegetation Hg uptake, or oceanic Hg emissions could explain this TGM increase. We then investigate the CHC TGM increase under the perspective of long-range transport coupled with interhemispheric exchange by combining Hg observations with Lagrangian transport modeling. We explore possibly important UT pathways for Hg interhemispheric transport over the tropical Pacific and tropical Indian oceans and investigate the role of interhemispheric exchange as driver of TGM seasonality in the SH tropical UT. Finally, we compare our results to CARIBIC observations on UT TGM and discuss the use of CHC TGM observations to evaluate interhemispheric Hg exchange in models.

2. Methodology

2.1. Chacaltaya Site Description

The Chacaltaya (CHC) regional GAW station (16.35023°S, 68.13143°W) lies at an altitude of 5,240 m asl. in tropical Bolivia (Andrade et al., 2015; Bianchi et al., 2022) (see Figure 3a, Figure S1 in Supporting Information S1), more than 1,000 m above but only ∼16 km away from the major urban agglomeration of La Paz/El Alto. CHC samples mostly free tropospheric air, but can be influenced by the planetary boundary layer of the surrounding Altiplano, mainly during daytime (Aliaga et al., 2021; Andrade et al., 2015; Chauvigné et al., 2019).

CHC is influenced by a seasonally varying mix of altiplanic and amazonian air masses (Aliaga et al., 2021; Chauvigné et al., 2019; Koenig et al., 2021), with mostly altiplanic influence in the dry season (around May–July) and stronger amazonian influence in the Wet season (December–March). CHC TGM is lowest in the dry season, rises during the BB season (August–October), and peaks in the early wet season. In the course of the wet season, CHC TGM declines again, likely as a result of vegetation Hg uptake in the Amazon basin. BB in the lowlands can enhance TGM at CHC, but this is mostly limited to the BB season (Koenig et al., 2021).

2.2. Atmospheric Mercury Measurements at Chacaltaya

Between July 2014 and February 2016 (20 months), TGM was continuously measured at CHC with a Tekran Model 2537A analyzer (Tekran Inc., Toronto, Canada), operating according to standard Global Mercury Observation System operating procedures (Munthe et al., 2011). Automatic calibration of the instrument was performed every 4 days through an internal Hg permeation source. Once a year, the automatic calibration was verified by manual injection of saturated mercury vapor, taken from a temperature-controlled vessel. The Teflon PFA (Perfluoroalkoxy alkanes) sampling line was UV protected and the inlet was installed at 6 m agl. Two 4.5 and 0.5 µm PTFE filters with diameter of 47 mm were installed between the Tekran and the inlet, preventing particulate matter from entering the detection system. The 2.5 m long sampling line was unheated. Considering the strong tendency of

gaseous oxidized mercury (GOM) to adsorb on a wide variety of surfaces, we acknowledge that some GOM wall loss might have occurred in the unheated sampling line, possibly leading to an underestimation of GOM (and hence TGM, defined as GEM + GOM) in ambient air. However, we expect the fraction of GOM wall loss to have been small, given that our air sampling configuration has been carefully designed to remove PBM and minimize any adsorption of GOM species in the sample line. Due to the low atmospheric pressure at this high-altitude site (~0.52 atm), the flow rate of the instrument was lowered from the typical 1.0 to 0.7 L min^{-1} at standard temperature and pressure (273.15 K, 1,013.25 hPa). This flow rate was permanently checked by an internal calibrated mass flow meter. Once every 3 months, the internal flow meter was itself manually checked and—if needed—recalibrated with an independent external volumetric flow meter. A clean time series was generated from raw Tekran data with special software developed at the Institute of Environmental Geosciences (see https://gmos.aeris-data.fr/, last access: 11 September 2021). During this automated process, a flag ("valid," "warning," or "invalid") was assigned to each TGM observation based on over 40 criteria linked to all phases concerning the instrument calibration and the calculation of TGM concentration (D'Amore et al., 2015). Based on this flagged data set, the site manager generated the final quality-insured and quality-controlled data set under consideration of field notes, logbooks, and site characteristics (Magand & Dommergue, 2022). A more detailed description of the CHC TGM measurement protocol can be found in Koenig et al. (2021).

2.3. ENSO Indices

The magnitude of El Niño events is regularly quantified through indices such as the Southern Oscillation Index (SOI), the Oceanic Niño Index (ONI), or the Multivariate ENSO Index (MEI). Here, we use all three indices as each of them expresses a different aspect of the ENSO perturbation. While the SOI is based on the pressure difference between Tahiti and Darwin, Australia, the ONI is based on the sea surface temperature anomaly in the Niño 3–4 regions (longitude range: 120°–170°, latitude range: 5°S–5°N). The MEI is a multivariate index that depends on sea level pressure, sea surface temperature, surface wind, and outgoing longwave radiation over the tropical Pacific (longitude range: 100°–70°, latitude range: 30°S–30°N). In contrast to monthly provided SOI and ONI, the MEI is provided in overlapping bi-monthly periods. To aid comparison to SOI and ONI, we calculated monthly MEI values by computing the arithmetic mean of overlapping bi-monthly periods.

Data on SOI, ONI, and MEI were obtained from https://psl.noaa.gov/enso/dashboard.html (last access: 10 September 2021).

2.4. Transport Modeling With HYSPLIT

2.4.1. HYSPLIT Back Trajectories to Estimate Air Mass History

We estimated long-range transport to CHC and adjacent regions on the seasonal timescale with HYSPLIT ("Hybrid Single-Particle Lagrangian Integrated Trajectory") back trajectories (Stein et al., 2015), using the HYSPLIT model in conjunction with the R library "splitr" (an R interface to HYSPLIT, https://github.com/rich-iannone/splitr, last access: 7 February 2022). We used the Global Data Assimilation System (GDAS1) as meteorological input due to its global and temporal coverage and manageable computational cost. Back trajectories were launched hourly from nine arrival points on a regular 0.5° × 0.5° (lat × lon) grid centered on CHC (see grid points in Figure S1 of Supporting Information S1). The starting altitude for all trajectories was 5,245 m asl., corresponding to 5 m above CHC mountain station. To account for the long-range transport, we chose a long run duration of 21 days, considerably longer than usually used in source attribution studies (<14 days, e.g., Gratz et al., 2015; Gustin et al., 2021; Jaffe et al., 2005). As there are large uncertainties in such long back trajectories (Riddle et al., 2006; Strode et al., 2008), we explicitly refrain from linking hourly TGM to individual trajectories and instead base all our results on large trajectory ensembles of at least 1 month worth of back trajectories (a 1 month ensemble is based on $\sim 9 \cdot 24 \cdot 30 = 6,480$ individual back trajectories).

Given the complex topography around the site and the long trajectory run duration, we do not expect that these GDAS1-based back trajectories adequately represent transport on the local and hourly or even daily scale, but we assume that back trajectory ensembles of 1 month or longer represent transport to CHC on synoptic and seasonal scale.

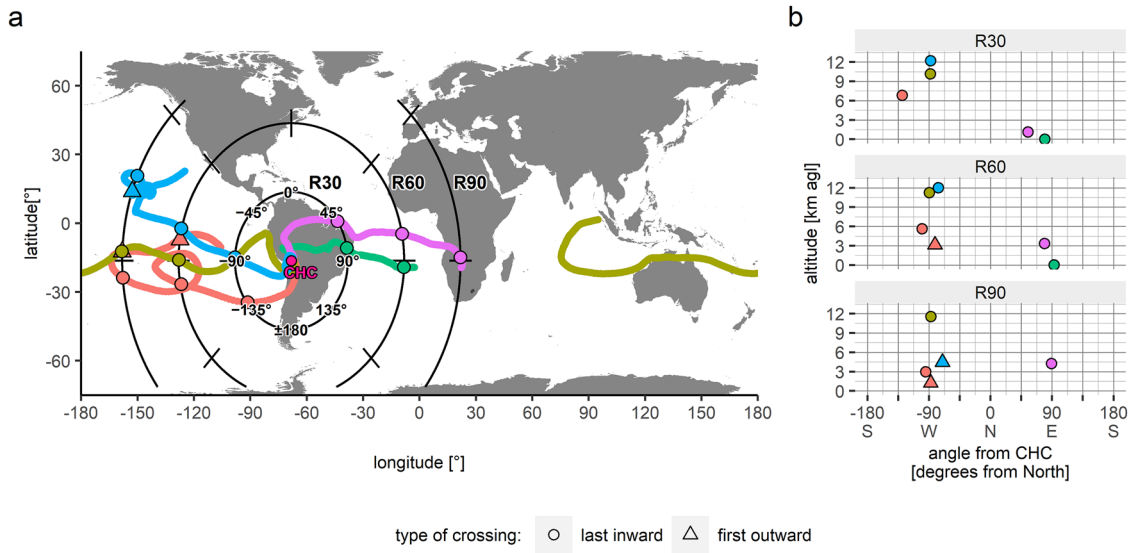


Figure 1. Illustration of the "cylindrical slices" approach used to characterize 3-D air mass origin. Five back trajectories were chosen as an example. (a) The black circles marked R30, R60, and R90 show three cylindrical slices corresponding to radii of 30, 60, and 90 geographical lat/lon degrees from CHC, respectively. Note that, given the spherical shape of the Earth, points on individual circles are not equidistant to CHC. Numbers show the angle from CHC in degrees (North = 0°). Circles and triangles indicate where a back trajectory crossed the respective cylindrical slice. (b) Back-trajectories in their representation on the cylindrical slices R30, R60, and R90. Each point on each surface indicates where the respective cylindrical slice was crossed by a back trajectory. Each trajectory can be represented by up to two different points on each cylindrical surface, corresponding to the last inward crossing (moving toward CHC) and the first outward crossing (moving away from CHC) of the cylindrical surface. While a trajectory can cross the same slice more than twice, this is very rare.

2.4.2. Cylindrical Slices and Definition of the "Upper Tropospheric Pacific Channel" (UTPC)

We summarized the vertical profile of air mass origin by creating what we call "cylindrical slices" from back trajectory ensembles. This procedure is schematized in Figure 1 and explained as follows: First, spatial coordinates (longitude, latitude, elevation) of CHC back trajectories were converted to a CHC-centered cylindrical coordinate system (a similar polar coordinate system was used in Aliaga et al. [2021] and Chauvigné et al. [2019]) defined by: radius to CHC, angle from CHC (North = 0°, South = ±180°), and elevation agl. We then defined a series of CHC-centered cylindrical surfaces $\{S_1, ..., S_n\}$ with radii $\{r_1, ..., r_n\}$. Interpreting these cylindrical surfaces as crosscuts through the 3-dimensional air mass origin defined by all back trajectories, we computed for each individual back trajectory the angle and elevation where it crossed each cylindrical surface S_i before arriving at CHC. In the rare case where one trajectory crossed a cylindrical slice multiple times, we included both first and last slice crossing (compare circles and triangles in Figure 1). This procedure of cylindrical slicing reduces each individual back trajectory to a series of points on the cylindrical surfaces $\{S_1, ..., S_n\}$ at discrete radii $\{r_1, ..., r_n\}$, allowing to represent 3-dimensional air mass origin in a series of 2-dimensional figures.

We used these cylindrical slices to characterize a likely important pathway of long-range transport to CHC, which we call the "UTPC". The UTPC represents air masses coming from the UT of the SH tropical Pacific, which may be particularly prone to be affected by interhemispheric exchange. To define and quantify the UTPC, we only considered the cylindrical slice at radius 60° (geographical lat/lon degrees) and assigned to the UTPC all back trajectories crossing this slice at any angle between −80° and −105° (0°, 90°, ±180° and −90° correspond to north, east, south, and west of CHC respectively) and any elevation between 4 km and 13 km agl (see Pink box in Figure 3b). This definition was based on the results from Section 3.3 and on Figure 3.

2.4.3. HYSPLIT Forward Trajectories to Estimate Interhemispheric North-to-South Transport

To investigate the interhemispheric Hg transport from NH to SH, defined here as the transport of Hg emitted north of the geographical equator to latitudes south of the geographical equator, we computed 21-day forward trajectories based on GDAS1. Forward trajectories were launched once a day from a regular 5° lat × 10° lon grid in the NH (latitudes: 10°N–30°N, longitudes: −180°–180°, starting altitude: 7,000 m asl., see grid points in Figure S2 of Supporting Information S1). To avoid bias by time zone differences, we randomized the hour of trajectory emission for each day and grid point. Forward trajectories were computed between February 2014 and August

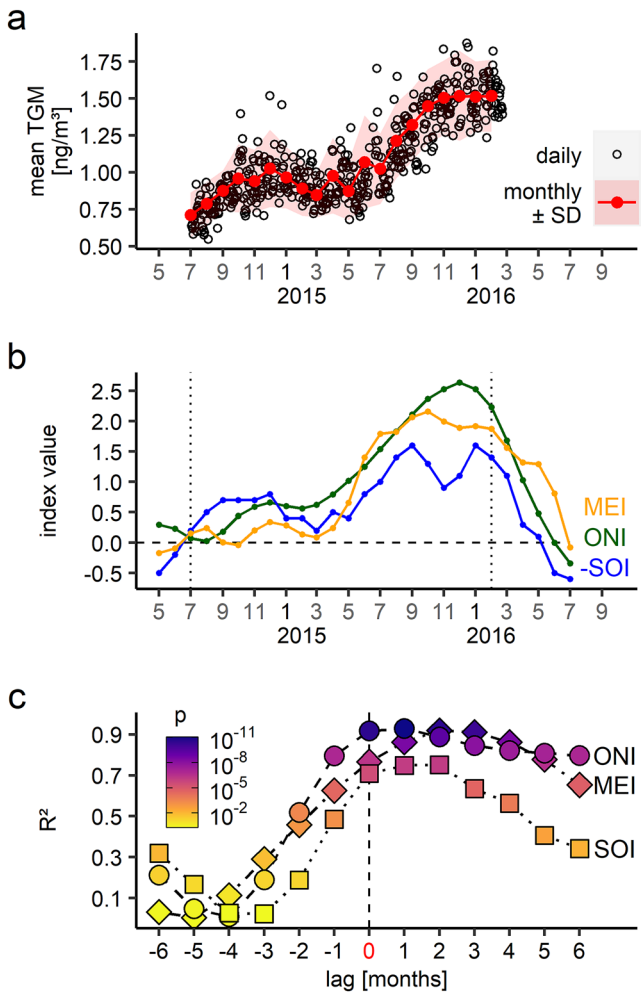


Figure 2. Chacaltaya (CHC) TGM observations and the onset of the 2015–2016 El Niño. (a) Steep increase of CHC TGM in 2015. Daily (monthly) arithmetic averages in black (red). Red shaded area: monthly average + −1 standard deviation. (b) Similar steep increase of ENSO indices (ONI, MEI, SOI) during the same months as in (a). SOI was multiplied by −1 to facilitate comparison between indices. The vertical dashed lines show the TGM measurement period. (c) CHC TGM lags behind ENSO indices by 1–2 months. We estimated the most likely time lag by computing R^2 (Pearson) between monthly TGM (a) and ENSO indices (b) for several lags. Positive (negative) lags mean that monthly TGM reacts after (before) the respective index.

2016. Similar to the CHC back-trajectories calculation (Section 2.4.1), the uncertainties in individual 21-day forward trajectories are large. We thus base all results on large forward trajectory ensembles, with the smallest ensemble used here (a 1 month ensemble) being composed of ∼5,400 (36 · 5 · 30) individual trajectories.

To estimate the magnitude of NH air masses flowing into the SH tropical UT (hereinafter: "NH air mass intrusion"), we applied a latitudinal threshold in the SH tropics, assuming that all NH-emitted forward trajectories that crossed this particular threshold latitude passed irreversibly to the SH and contributed to interhemispheric exchange. Here, we chose 15°S as threshold latitude, as it closely resembles the latitude of CHC (16.35°S) and should lie throughout the year south of the intertropical convergence zone (Schneider et al., 2014). While the exact choice of this threshold latitude is somewhat arbitrary, we verified that our results and conclusions are insensitive to this threshold (sensitivity analysis in Figures S3 and S4 in Supporting Information S1).

To obtain a time series representing the seasonal and interannual variation of NH air mass intrusion into the SH UT, and thus the UTPC, we counted for each month of the year the number of forward trajectories (emitted in the NH) that crossed the threshold latitude of 15°S at any elevation above mixing height (as given by GDAS1). We then normalized this time series through min-max normalization, so that values of "1" and "0" correspond to the month with strongest (weakest) UT north-to-south transport, respectively.

2.5. Linking Long-Range Transport to CHC TGM

2.5.1. Linear Model Equation 1—Transport Term Only

To establish an algebraic expression for the relationship between TGM measured at CHC and air masses coming from the UTPC, we used the following approach: We began with a box model equation (See Text S1 and Equation 1 in Supporting Information S1), assuming that CHC TGM is representative of a region with unknown but constant spatial extent, enclosing a constant volume of air. We furthermore assumed that (a) the volume of air entering this region after passing through the UTPC is directly proportional to the HYSPLIT-derived UTPC influence (Figure 3c) and (b) that TGM in the UTPC is either constant or following an unknown temporal variation. We did not make steady-state assumptions (i.e., $dTGM/dt \neq 0$). Upon developing the box model equation under these assumptions, we obtained Equation 1, which establishes a linear relationship between the relative UTPC influence (the fraction of emitted HYSPLIT back-trajectories that passed through the UTPC before arrival at CHC; constrained between 0 and 1) and CHC TGM concentrations through their first temporal derivative ($dTGM/dt$ in ng m^{-3} day^{-1}). The full development can be found in Text S1 in Supporting Information S1.

$$dTGM/dt(t) = c\,a \cdot \mathrm{UTPC}(t) + b + f(t) \quad (1)$$

Here, c is a constant TGM concentration in the UTPC (in ng m^{-3}), a is a dimensionless constant of proportionality between the volume of air getting transported into the box (the region represented by CHC) and the unknown total volume of air within the box (see Equation 8 in Supporting Information S1), and b is a constant (in ng m^{-3} day^{-1}). The function f is an unknown time-dependent function, and the sum $b + f(t)$ contains the unknown temporal variation of UTPC TGM, as well as all terms in the box model equation not directly linked to transport through

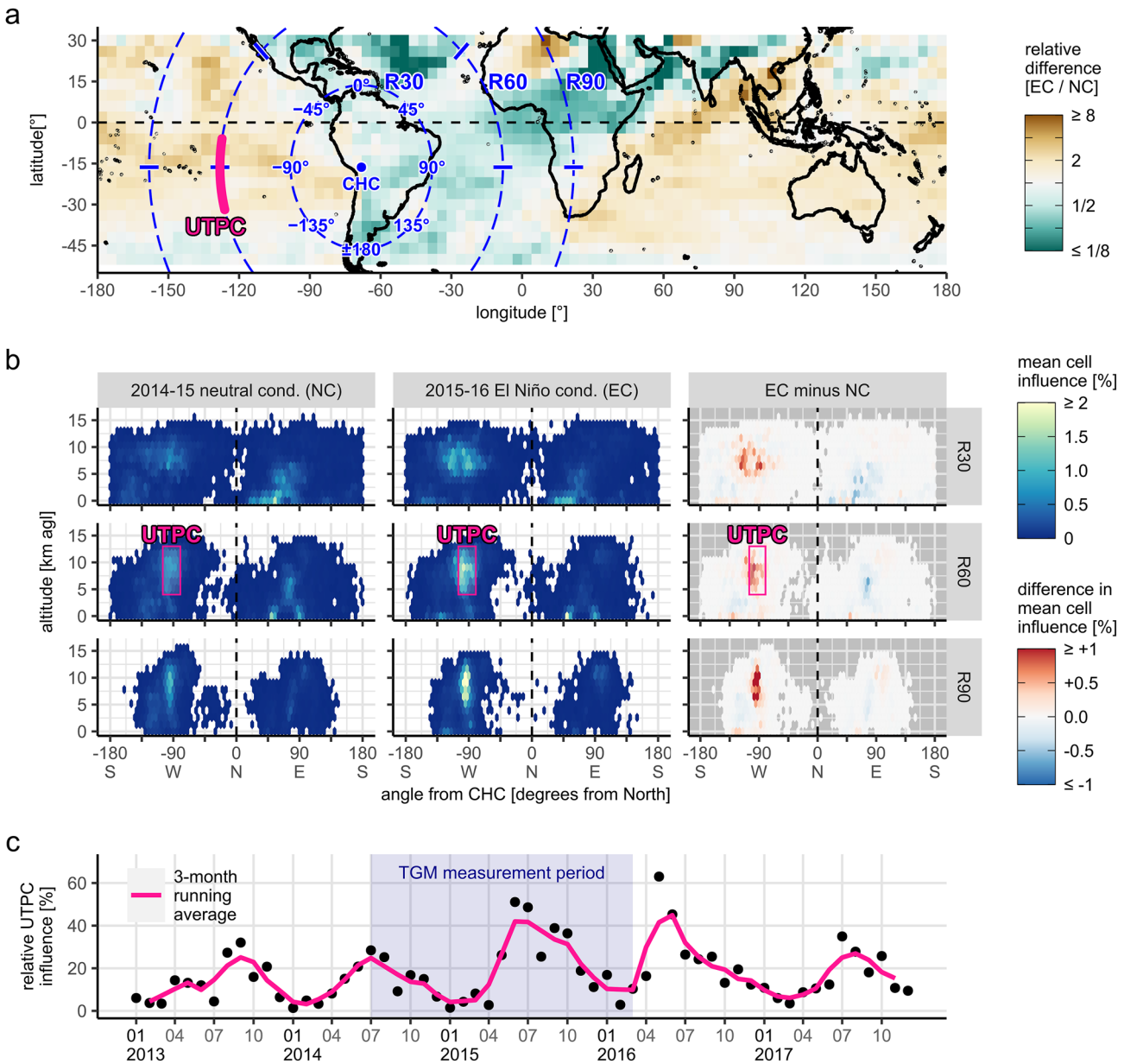


Figure 3. Westwards shift in Chacaltaya (CHC) air mass origin in 2015–2016 as characterized by 21-day HYSPLIT back trajectories. (a) Relative difference in source region influence between "2014–2015 neutral conditions" (NC, here May 2014 to April 2015) and "2015–2016 El Niño conditions" (EC, here May 2015 to April 2016), defined as the total number of HYSPLIT trajectories crossing a grid cell during EC divided by the total number of HYSPLIT back trajectories crossing the same grid cell during NC. The dashed circles (R30, R60, and R90) show three cylindrical cross-cuts corresponding to radii of 30, 60, and 90 geographical lat/lon degrees from CHC, respectively. Note that points on individual circles are not equidistant to CHC due to the spherical shape of the Earth. Blue numbers show angle from CHC in angular degrees (North = 0°). The definition of the UTPC is given as pink arc (see also (b)). (b) Altitude profiles of CHC air mass origin during NC, EC, and their difference, at selected radii from CHC (dashed circles in (a)). These altitude profiles are based on "cylindrical slices", by which we reduce each HYSPLIT back trajectory to points on cylindrical cross-cut surfaces (see Section 2.4.2, Figure 1). The mean cell influence was defined as the percentage of all back trajectories emitted from CHC that crossed the respective cell on the cylindrical surface during their 21-day run duration. Most El Niño-anomalies in westerly transport can be narrowed down to a relatively narrow mid-to-upper tropospheric "channel", which we define as "upper tropospheric pacific channel" (UTPC, pink arc in (a)). (c) Evolution of relative UTPC influence, defined as percentage of all emitted 21-day back trajectories that passed through the UTPC before reaching CHC. The influence of the UTPC varies seasonally and was amplified in 2015–2016.

the UTPC, such as the emission term, the sink term, and the term expressing TGM getting transported out of the box (See Equation 9 in Supporting Information S1).

Equation 1 is suitable to compute a linear fit of the form $y = ax + b +$ residuals. The unknown function $f(t)$ is expressed in the fit residuals. Large residuals (low R^2) in a fit following Equation 1 suggest that $f(t)$ dominates and that the time variation in TGM/dt is better explained by other (here not explicitly resolved) drivers than by the transport through the UTPC, while low residuals (high R^2) suggest the opposite. We highlight that following Equation 1, there is no direct linear relationship between CHC TGM and UTPC influence. Instead, the UTPC influence relates linearly to the first temporal derivative of TGM measured at CHC ($dTGM/dt(t)$). This is a result of non-equilibrium conditions ($dTGM/dt \neq 0$) and the inertia of the system, which takes time to react to changes in fluxes (e.g., reservoirs need time to fill or empty).

2.5.2. Model Equation 3: Including Interhemispheric Transport as Driver for UTPC TGM Seasonality

We hypothesize that the seasonality of UTPC TGM is driven by the seasonality of NH air mass intrusion into the SH tropics, that is, that UTPC TGM is strongly driven by interhemispheric exchange. Under this hypothesis, we further developed Equation 1 by expressing the seasonality of UTPC TGM as a function of NH air mass intrusion into the UTPC as estimated with HYSPLIT forward trajectories (see Section 2.4.3). To represent the latter, we derived a univariate time series by zonal integration of NH air mass intrusion at 15°S and subsequent min-max normalization (see Section 2.4.3 and Figure 5c). We propose a linear relationship between TGM in the UTPC (c_U) and the aforementioned normalized time series for NH intrusion into the UTPC (IH):

$$c_U(t) = c_0 + e\,IH(t-l) \tag{2}$$

where c_0 is a constant TGM baseline concentration (in ng/m^3) and l is a time lag (in months). This time lag l addresses (a) the transport time from the UTPC to CHC (around 10 days, see Figure S5 in Supporting Information S1) and (b) the possibility that UTPC TGM, an integrated quantity, peaks after the interhemispheric transport flux IH, as the UT reservoir represented by the UTPC may need time to fill.

By implementing this expression for UTPC TGM (Equation 2) into Equation 1, we derived Equation 3 (full development in Text S2 of Supporting Information S1). Equation 3 links CHC $dTGM/dt(t)$ not only to the UTPC influence on CHC but also to the estimated NH air mass intrusion into the UTPC.

$$dTGM/dt(t) = c_o a\,\mathrm{UTPC}(t) + ea\,\mathrm{UTPC}(t)\,IH(t-l) + b + f^*(t) \tag{3}$$

Resembling f in Equation 1, $f^*(t)$ in Equation 3 is an unknown time-dependent function that, for a linear model, is reflected in the fit residuals. The values of coefficients ea and $c_0 a$ in Equation 3 are not easily interpretable given the unknown scaling factor a. However, their ratio simplifies to e/c_0, which is the ratio between the amplitude of seasonal TGM variation and constant baseline TGM in the UTPC (see Equation 2), giving information about the magnitude of seasonal variability.

We assumed in Equation 1 that the volume of air coming from the UTPC is proportional to the number of HYSPLIT back trajectories passing through the UTPC before arrival at CHC. Similarly, in Equation 3 we assumed proportionality between the volume of air flowing from the NH to the SH and the normalized number of HYSPLIT trajectories crossing the threshold latitude at 15° from North to South (IH). While unlikely universally true, we argue that these assumptions should hold well enough on the seasonal timescale, and if a large ensemble of back trajectories is considered.

We did not include chemical transformations and removal of TGM during transport, neither in Equation 1 nor in Equation 3. We justify this choice with the long atmospheric lifetime of TGM (~5.2 months–1.7 yr, see introduction) in comparison to the transport times considered here, with ~10 days from UTPC to CHC (Figure S5 in Supporting Information S1) and <2 months for the whole transport pathway from NH UT to CHC.

We highlight that, considering the large uncertainties in Hg drivers in South America, Hg redox chemistry, as well as Hg oxidant concentrations (see introduction), we made no attempt to build a complete model to fully explain CHC TGM, and Equations 1 and 3 should not be interpreted as such. The box model equation is merely used as a starting point to (a) deduce an adequate theoretical relationship between CHC TGM and UTPC, and (b) investigate how CHC TGM relates to a seasonality in UTPC TGM.

2.6. Calculation of *dTGM/dt* With Smoothing Splines

The derived equations Equations 1 and 3 link UTPC influence not to CHC TGM concentrations directly but to their first temporal derivative ($dTGM/dt$) instead. This made it necessary to obtain $dTGM/dt$. We estimated $dTGM/dt$ on a monthly timescale with cubic smoothing splines, a technique that has been proven adequate for obtaining high-quality derivatives of experimental data, being more reliable than the finite-difference approach (Berghaus & Cannon, 1973). After removing 6 days of data (24 June 2015 to 29 June 2015) that were clearly influenced by the "San Juan" regional anthropogenic pollution event (Koenig et al., 2021), we computed daily TGM averages and filled data gaps with a 30-day running median. On this gapless daily averaged time series, we fitted cubic smoothing splines (function *smooth.spline()* from base R 3.6.0; 125 knots).

A smoothing spline depends on the chosen smoothing parameter. The stronger the spline smoothing, the more high-frequency variations in the data get suppressed, comparably to a low-pass filter. As the choice on the spline smoothing parameter impacts the results (Berghaus & Cannon, 1973), we took an ensemble approach to minimize the subjectiveness in the choice of the spline smoothing parameter and to quantify uncertainties. We created an ensemble of smoothing splines from a range of different smoothing parameters k (in this R-specific case: *spar* ranging from 0.8 to 1.0 in increments of 0.001) giving rise to a total of 201 individual smoothing splines S_k. We confirmed visually that CHC TGM was, on a seasonal timescale, well represented by the ensemble of S_k (see Figure S6 in Supporting Information S1). We then analytically derived each S_k and calculated its monthly average to obtain an individual monthly time series $(dTGM/dt)_k$. Finally, we took the ensemble median of all $(dTGM/dt)_k$ as our best estimate of CHC $dTGM/dt$. As 95% confidence interval of $dTGM/dt$, we used the 2.5th and 97.5th percentiles of the distribution of $(dTGM/dt)_k$. To limit edge effects arising from the calculation of the first derivative, we excluded both the first and last monthly average of the obtained $dTGM/dt$ time series from further analysis (see Figure S6b in Supporting Information S1).

2.7. Comparison to CARIBIC Data

Making use of the CHC TGM increase in 2015, we estimated the seasonality of TGM in the UTPC. To validate this remotely reconstructed seasonality, we compared it to aircraft TGM observations in the SH tropical UT. We used IAGOS CARIBIC data taken on civil aircraft flights between June 2005 and March 2016, selecting only flights connecting to destinations in SH South America (36 individual flights). To constrain TGM seasonality in the SH UT as close to the UTPC as possible, we selected only CARIBIC TGM measured at altitudes above 4,000 m asl., within latitudes 25°S–5°S (the threshold latitude for NH air mass intrusion at 15°S ± 10°), and longitudes −50° to −30°. We then summarized by month of the year to maximize available data and to focus on the mean TGM seasonality. The seasonality of UT carbon monoxide, based on the same data selection, is shown in Figure S7 of Supporting Information S1.

3. Results and Discussion

3.1. The CHC TGM Increase During the 2015–2016 El Niño

TGM at CHC rose strongly in 2015, reaching about 50% higher mean concentrations in November–December 2015 (1.54 ng/m^3, SD: 0.28 ng/m^3) compared to November–December 2014 (0.98 ng/m^3, SD: 0.24 ng/m^3; Figure 2a). The lower TGM concentrations in 2014 appear to represent more typical Hg concentrations in this region, as Hg^0 of below 1 ng/m^3, similar to CHC TGM in 2014, was measured at the Titicaca lake (~110 km north-west of CHC; Guédron et al., 2017) and at two background sites in the Peruvian "Madre de Dios" region (~800 km north-west of CHC; Gerson et al., 2022). On the other hand, the elevated TGM concentrations at CHC during 2015–2016 represent—to our knowledge—the first time that monthly mean atmospheric Hg concentrations of over 1.5 ng/m^3 have been observed at a background site in the SH (other than Antarctica).

To investigate the timing of the CHC TGM increase in relation to the onset of the 2015–2016 El Niño, we compared CHC TGM to three widely used ENSO-indices: The ONI, SOI, and MEI (see Section 2.3). We found that TGM increased nearly synchronously with the developing El Niño as characterized by these indices, albeit slightly lagging behind them (Figures 2a and 2b). We estimated the most likely time lag between CHC TGM and the onset of the 2015–2016 El Niño by computing the Pearson correlation between monthly averaged TGM

and the three ENSO indices at different lags (Figure 2c): CHC TGM lagged about 1 month behind the ONI, 2 months behind the SOI, and 2 months behind the MEI, with corresponding R^2 of 0.93, 0.75, and 0.92 respectively. However, this good temporal coincidence gives no explanation on what happened in particular in 2015 that caused TGM to rise. Two plausible hypotheses, enhanced BB and suppressed vegetation Hg^0 uptake, are explored in the following.

3.2. The Potential Role of BB in South America and Suppressed Vegetation Uptake in the Amazon

It is known that BB can emit large amounts of Hg into the atmosphere and that ENSO can impact the magnitude of wildfires in the tropics (Y. Chen et al., 2011; Liu et al., 2017). Indeed, Slemr et al. (2016) found an ENSO-related signal in CARIBIC Hg data, which they attributed mainly to enhanced BB emissions during El Niño conditions. Besides, TGM measured at CHC can be influenced by BB in the lowlands, especially in the BB season (~August until late October; Koenig et al., 2021). However, we find that BB in South America is unlikely the main driver of the CHC TGM increase during this particular El Niño as this is not supported by CHC carbon monoxide (CO) and black carbon (BC) observations, which did not show an increase in 2015 comparable to that of TGM. Reported BB-related TGM/CO emission ratios are usually below ~0.002 ng/m^3 (Ebinghaus et al., 2007; McLagan et al., 2021; Wang et al., 2015) and were for the CHC-specific case determined to be between 0.0014 and 0.0024 $\left(\text{ng m}^{-3}\right)_{\text{TGM}}$ /$(\text{ppbv})_{\text{CO}}$ for air masses of Amazonian origin (Koenig et al., 2021). Considering such TGM/CO emission ratios, we would expect to observe a simultaneous and very large CO increase of around 200 ppbv to justify attributing the large CHC TGM increase (>0.5 ng/m^3) to increased BB in South America. In contrast, mean CHC CO was near identical in 2015 (121 ppbv; SD: 21 ppbv) and 2014 (117 ppbv; SD: 26 ppbv) and CHC BC was also not importantly enhanced (Figures S8 and S9 in Supporting Information S1), rendering the BB hypothesis unlikely.

Similarly, a change in vegetation Hg^0 uptake also appears unlikely as the main driver for the observed TGM increase. It has been shown that vegetation acts as a net sink for atmospheric Hg^0 by foliar uptake (Jiskra et al., 2018; Zhou et al., 2021). In the specific case of CHC, a vegetation-related TGM decrease has been detected in air masses coming from the Amazon rainforest during the growing season (Koenig et al., 2021). As the 2015–2016 El Niño significantly reduced gross primary production of the Amazon rainforest (see introduction), it most likely also reduced its vegetation Hg uptake. Such a reduction in vegetation Hg uptake would unbalance Hg sources and sinks and potentially increase atmospheric Hg in the region. Hence, one would expect Hg to start rising shortly after the vegetation uptake anomaly begins. The timing of the vegetation uptake anomaly in 2015–2016 does however not agree with the CHC Hg increase: for all major regions of the Amazon basin, the vegetation sink did not deviate from the multiyear mean until around October 2015, and was most anomalous recently around November–December 2015 (Koren et al., 2018). In September 2015, weeks before the vegetation sink anomaly started manifesting, mean CHC TGM was already ~50% (0.45 ng/m^3) higher than the same time the year before (Figure 2a). This large TGM increase before October 2015 cannot be attributed to the reported vegetation sink anomaly in 2015–2016. That said, suppression of the Amazon rainforest vegetation sink toward late 2015 could explain why CHC Hg did not decrease during the 2015–2016 wet season (December–March), in contrast to the 2014–2015 wet season where such a decrease was clearly observable (Figure 2a).

3.3. Change in Air Mass Origin in 2015–2016

Hg, especially in its elemental form, is transported over long distances in the atmosphere, and observed Hg concentrations can be strongly impacted by atmospheric transport (Schroeder & Munthe, 1998; Strode et al., 2008). To investigate changes in the long-range transport to CHC, we used HYSPLIT back trajectories (see Section 2.4.1).

We found an important shift in long-range transport to CHC in 2015–2016. Compared to the year before (2014), the influence of the Pacific sector on CHC was amplified in 2015–2016, while the influence of continental South America and the Atlantic sector was diminished (Figure 3a). There was a general westward shift in CHC air mass origin, which was most prominent in the UT (Figure 3b). To quantify this westerly UT transport pathway, we defined the "upper-tropospheric Pacific Channel" (UTPC; see Section 2.4.2). Conceptually, the UTPC represents air masses from the UT of the SH tropical Pacific. In practice, we assigned to the UTPC all back trajectories passing through the pink arc and pink rectangle shown in Figures 3a and 3b, respectively (see Section 2.4.2). UTPC influence on CHC shows a regular seasonality, usually peaking between July and August (Figure 3c). However, in

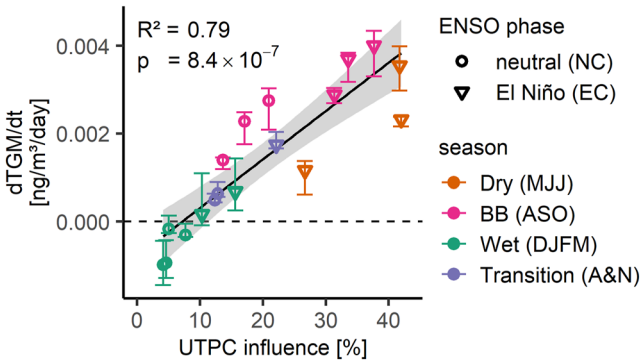


Figure 4. Fit results following Equation 1. There is a significant positive linear relationship between monthly UTPC influence (3-month running average) and monthly CHC *dTGM/dt*. Error bars give 95% confidence intervals. "2015–2016 El Niño conditions" (EC) from May 2015 to April 2016 and "2014–2015 neutral conditions" (NC) from May 2014 to April 2015. There is a seasonal pattern in fit residuals: *dTGM/dt* is systematically underestimated in the BB season and overestimated in the wet season. The largest residuals fall into the dry season.

2015–2016, UTPC influence on CHC was highly amplified: between June and October 2015, around 40% of all air masses arriving at CHC came from the UTPC. This is about twice as much as the year before (2014), which, regarding UTPC influence, is similar to the years 2013 and 2017 and appears representative of normal conditions (Figure 3c).

3.4. A Link to Long Range Transport

Above, we showed that CHC experienced a westward shift in air mass origin in 2015–2016, with a strongly enhanced influence of the UTPC. In the present section, we explore how the CHC TGM increase relates to the UTPC.

We derived an algebraic expression (Equation 1), according to which the HYSPLIT-derived UTPC influence should not be compared to TGM concentrations at CHC directly, but to their first temporal derivative ($dTGM/dt$) instead (see Section 2.5.1). We obtained a suitable monthly averaged $dTGM/dt$ time series by using cubic smoothing splines (see Section 2.6). This time series shows enhanced $dTGM/dt$ in 2015, with around 45% higher $dTGM/dt$ in August 2015 as compared to August 2014 (see Figure S6b in Supporting Information S1).

Computing a linear fit based on Equation 1, we found a strong linear relationship ($p = 8.4 \times 10^{-7}$, $R^2 = 0.79$) between CHC $dTGM/dt$ (see Figure S6b in Supporting Information S1) and UTPC influence (pink line in Figure 3c), suggesting that enhanced UTPC influence alone can explain the magnitude of the TGM increase in 2015 (Figure 4). When UTPC influence on CHC increases, the influence of other air mass source regions decreases, such as continental South America and the Atlantic sector (see Figures 3a and 3b). As enhanced UTPC influence is associated with rising CHC TGM, these results suggest that TGM is higher in the UTPC than in these other source regions and more generally the SH background.

The linear relationship between $dTGM/dt$ and UTPC influence is significant. However, we find a seasonality in Equation 1 fit residuals (Figure 4, see also Figure S10 in Supporting Information S1), with systematically underestimated $dTGM/dt$ in the BB season (August–October), overestimated $dTGM/dt$ in the wet season (December–March) and largest residuals in the dry season (May–July). This seasonality in fit residuals gives insights about the unknown function f in Equation 1 and suggest either uncaptured seasonal drivers of CHC $dTGM/dt$, uncaptured seasonality of UTPC TGM, or a combination of both.

3.5. The Potential Role of Oceanic Emissions From the SH Tropical Pacific

Our above results suggested that TGM concentrations in the UTPC are elevated compared to the SH background. This raises the question on which process could drive enhanced UTPC TGM.

The westward shift in air mass origin for CHC in 2015–2016 (Figure 3) is consistent with an eastward shift of the Pacific Walker circulation typically associated to El Niño conditions, which can enhance convection over the central equatorial Pacific and favor the transport of air masses from the pacific sector to tropical South America (see introduction). It is thus a plausible hypothesis that CHC TGM rose in 2015 due to increased eastward transport of surface emissions from the SH Pacific Ocean, likely through the UTPC.

However, it appears that the increase in westerly transport to CHC was mainly restricted to the UT and included little surface air from the SH Pacific Ocean, at least for the last 21 days before arrival at CHC (Figure 3). In contrast to UT air masses that mostly move eastwards, surface air from the SH tropical Pacific, at least south of ~10°S, tends to get transported westwards by trade winds (Figure S11 in Supporting Information S1), even if the latter are admittedly weakened during El Niño. If these surface air masses carried with regularity as elevated Hg as CHC data would suggest (~1.5 ng/m^3), either in 2015–2016 or before, it should be reflected in Hg observations at the coastal ATARS site in northern Australia (see introduction, Figure S12 in Supporting Information S1). Yet, this is not supported by ATARS Hg: Gaseous elemental mercury at ATARS was only ~1 ng/m^3 between 2014 and 2016, and not impacted by the 2015–2016 El Niño (Howard et al., 2017). Exceptionally high ATARS Hg was

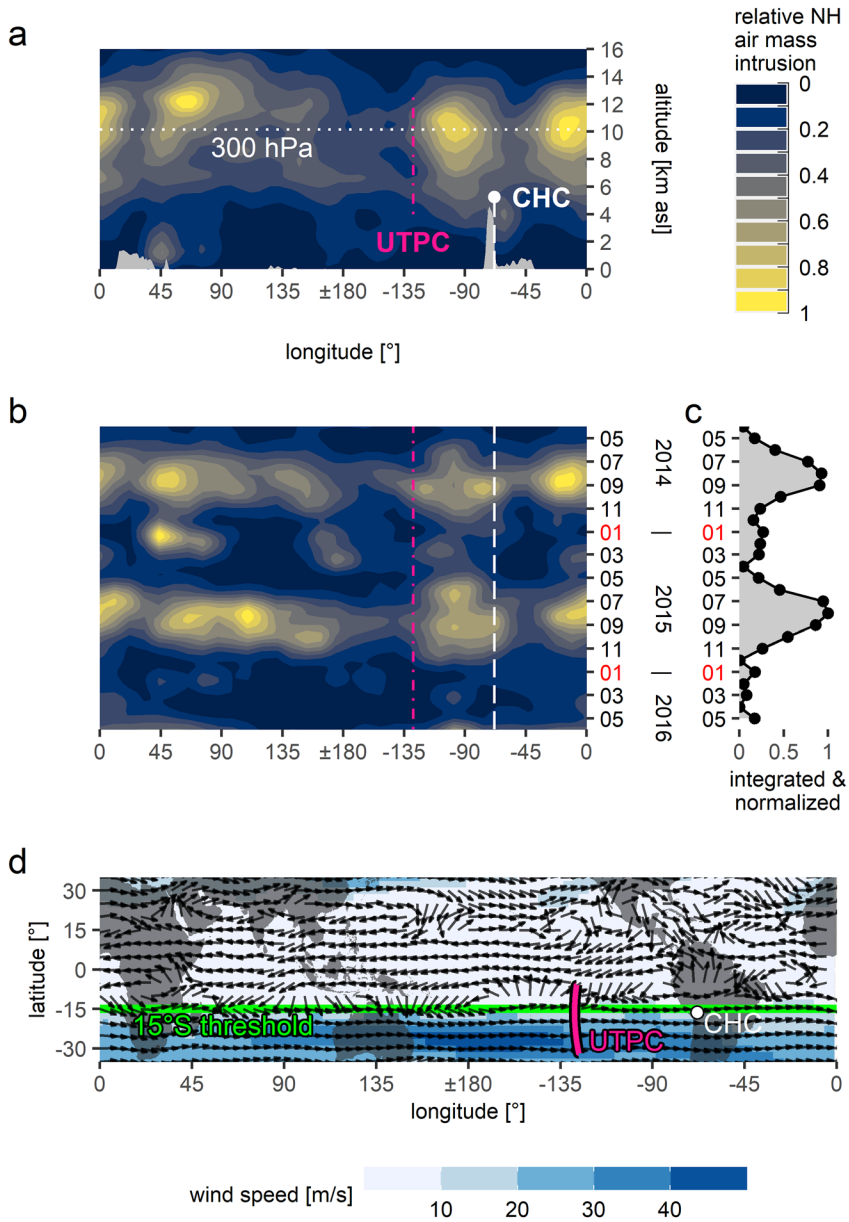


Figure 5. Pathways and seasonality of Northern Hemisphere (NH) air mass intrusion as estimated by 21-day HYSPLIT forward trajectories: (a) altitude profile of the relative magnitude of NH air mass intrusion into the Southern Hemisphere (SH) tropics. Magnitude of NH air mass intrusion estimated by counting how many HYSPLIT forward trajectories emitted in the NH crossed the threshold latitude 15°S (compare to green line in (d)) during their 21-day runtime (all forward trajectories between February 2014 and August 2016). NH air mass intrusion occurs preferentially in the mid-to-upper troposphere (UT), approximately between 6 km and 14 km asl. Three preferred longitudinal bands for NH air mass intrusion emerge, centered around the longitudes 60°, −90°, and −10°. Terrain altitude from the HYSPLIT digital elevation model at the 15°S intersection is shown in gray. (b) Temporal evolution of NH air mass intrusion at 15°S (at altitudes above mixing height as taken from GDAS1, see Section 2.4.3). NH air mass intrusion shows a marked seasonality, with the strongest magnitude between July and September. For the longitudes 100°–170°, NH air mass intrusion appears somewhat enhanced in 2015, as compared to 2014. (c) Estimated temporal evolution of NH air mass intrusion into the global SH tropical UT, obtained by zonal integration of panel (b) and min-max normalization. (d) NCEP/NCAR reanalysis wind vector fields at 300 hPa (compare to dotted line in (a)) between June 2015 and October 2015 reveal fast eastward transport in the SH tropical UT. Wind vector length is independent from wind speed, which is color-coded instead. Pink arc shows definition of the UTPC. The 15°S threshold latitude 15°S where NH air mass intrusion was estimated (for panels (a–c)) is shown as green line.

near-exclusively linked to northerly equator-crossing air masses and not to easterlies from the SH tropical Pacific. In another line of evidence, a recent modeling study suggests that atmospheric Hg variations in South America as consequence of ENSO-related anomalies in oceanic emissions do usually not exceed ∼5% of the multiyear mean, and that potential positive concentration anomalies recently manifest after the peak of El Niño (Huang & Zhang, 2021). They also estimated that during the 2015–2016 El Niño in particular, oceanic Hg emissions from the equatorial or SH tropical Pacific were reduced, not increased, mainly due to a reduction in surface wind speeds (Huang & Zhang, 2021 and corresponding Supporting Information).

We thus consider it unlikely that oceanic surface emissions from the equatorial or SH tropical Pacific Ocean are the main drivers of elevated TGM in the UTPC and, by extension, the TGM increase at CHC.

3.6. Interhemispheric Exchange Driving TGM in the UTPC

We have so far reasoned that the large TGM rise at CHC was unlikely caused by BB in South America and changes in the Amazon vegetation sink. Instead, we found that this TGM increase could be explained by a westward shift in long-range transport coupled with elevated TGM in the UTPC. We then argued that elevated UTPC TGM is unlikely driven by oceanic emissions from the equatorial or SH tropical Pacific, leaving the main driver yet to be determined.

It has been shown in previous work that the transport of NH air to the SH mostly happens in the tropical UT, and that interhemispheric exchange exhibits a strong seasonality (see introduction). It is noteworthy that the UTPC represents air masses coming from the SH tropical UT in particular, and that our results suggested a yet unidentified seasonality of TGM in the UTPC (see Section 3.4). We also note that the mean interhemispheric atmospheric Hg gradient is around 0.5 ng/m^3 (Travnikov et al., 2017), which is remarkably similar to the CHC TGM increase in 2015 (Figure 2a). This leads us to our main hypotheses that (a) elevated TGM in the UTPC (in comparison to the SH background) is mainly driven by NH to SH interhemispheric transport and that (b) the seasonality of UTPC TGM is closely linked to the seasonality of NH air mass intrusion into the SH.

To explore this hypothesis, we first addressed and quantified pathways and seasonality of interhemispheric transport from the NH into the SH tropics by using HYSPLIT forward trajectories, emitted from a regular grid in the NH UT. As metric of NH air mass intrusion into the SH, we calculated when and where these trajectories crossed the threshold latitude of 15°S from north to south (see Section 2.4.3).

In agreement with previous studies (see introduction), we find that NH air mass intrusion into the SH tropics occurs primarily in the tropical UT, between around 6 and 14 km asl (Figure 5a). This corresponds well to the defined UTPC altitude range (4–13 km agl). Globally, three major nodes of interhemispheric north-to-south transport emerge, approximately centered around the longitudes of 60°, −90°, and −10°. Once crossed from the NH to the SH tropics, air masses can get caught in a strong zonal westerly flow that is especially rapid over the tropical Pacific Ocean (Figure 5d). Seen from CHC, this transport pathway should be captured by the UTPC, recalling that the UTPC was defined to represent an UT westerly flow coming from the SH tropical Pacific UT (see Figure 3). We, therefore, find that NH air intrusion into the UTPC likely occurs.

We obtain a pronounced seasonality for UT NH air mass intrusion, with the strongest magnitude between July and September (Figures 5b and 5c). This result is in good agreement with previous model studies, who found a similar seasonality of UT interhemispheric exchange (Bowman & Cohen, 1997; G. Chen et al., 2017; Miyazaki et al., 2009; Newell et al., 1969; Yan et al., 2021). We find that this seasonality of interhemispheric exchange was apparently not altered in 2015. While the total magnitude of global UT NH air mass intrusion into the SH tropics seems quite similar in 2015 and 2014 (Figure 5c), there appears to have been some increase in UT NH air mass intrusion in the longitude range 100°–170°, corresponding approximately to the eastern Indian Ocean, South-East Asia and the western Pacific (Figure 5b), highlighting the importance of the Asian Summer monsoon in interhemispheric exchange (Yan et al., 2021).

3.7. Linking the Interhemispheric Transport Hypothesis to CHC TGM

We hypothesized that interhemispheric transport from NH to SH enhances TGM in the UTPC and drives UTPC TGM seasonality, which we characterized and quantified using HYSPLIT forward trajectories.

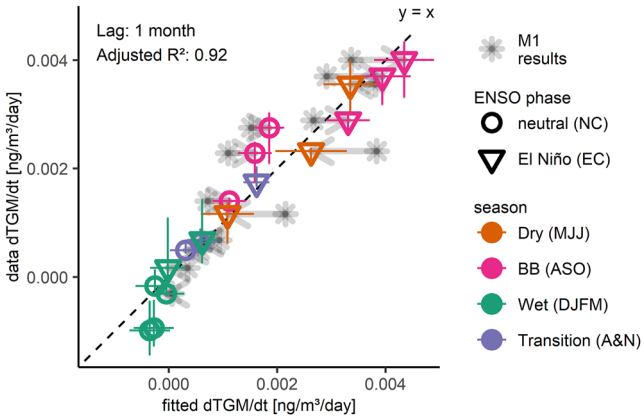


Figure 6. Significant improvement of *dTGM/dt* prediction by the inclusion of interhemispheric exchange. Fit based on Equation 3, assuming a lag of 1 month between TGM in the UTPC and upper tropospheric interhemispheric transport (hence UTPC TGM peaking in September). Error bars show 95% confidence intervals. "2015–2016 El Niño conditions" (EC) from May 2015 to April 2016, "2014–2015 neutral conditions" (NC) from May 2014 to April 2015. Dashed line gives the 1:1 reference. Stars show fitted values as obtained by the fit following Equation 1 (M1). Arrows indicate how fitted values changed from M1 to the best fit following Equation 3 (M2), thus visualizing the effect of including the seasonality of NH air mass intrusion into the fit. In contrast to M1, there is no seasonal pattern in the residuals of fit M2.

To test this hypothesis, we assume that UTPC TGM depends linearly on the magnitude of total NH air mass intrusion into the SH tropics, but permitting some lag between the two as the UTPC TGM reservoir may need time to fill (Equation 2, see Section 2.5). Further developing our first linear expression (Equation 1) under this assumption yields a new algebraic expression (Equation 3), which now relates CHC $dTGM/dt$ not only to the UTPC influence, but also to NH air mass intrusion into the SH tropics (see Section 2.5.2).

The lag between UTPC TGM and the magnitude of NH air mass intrusion is unknown but necessary to compute Equation 3. As solution, we computed the Equation 3-based multilinear regression for a range of time lags and determined the most likely lag by an exclusion principle: we excluded all those lags as possible solutions for Equation 3 that led to fit coefficients statistically not significantly different from zero ($\alpha = 0.025$). After application of this exclusion principle, only two valid fits remained, corresponding to lags of 1 and 2 months and giving adjusted R^2 of 0.92 and 0.86 respectively (see all fit results in Table S1 in Supporting Information S1).

The excellent fit for a lag of 1 month as the most likely solution for Equation 3 is shown in Figure 6 (see Figure S13 in Supporting Information S1 for all other fits). We find that including interhemispheric transport as driver for UTPC TGM seasonality (Equation 3, Figure 6) allows to explain observed CHC $dTGM/dt$ variation and thus the CHC TGM increase significantly better than assuming constant UTPC TGM (Equation 1, Figure 4). This adjustment significantly increases the adjusted R^2 of the fit (0.92 for the best fit following Equation 3 (M2) vs. 0.79 for the fit following Equation 1 (M1); $\alpha = 0.05$) and the seasonal pattern of residuals observable for M1 (Figure 4, Figure S10 in Supporting Information S1) vanishes in M2 (Figure 6). This suggests that the seasonality of TGM in the UTPC can be adequately expressed in function of NH air mass intrusion into the global SH UT. While these results are based on HYSPLIT trajectories of unusually long run time (21 days), we found that our results and conclusions are virtually unchanged if a shorter trajectory runtime is chosen (down to 10 days, sensitivity analysis in Figure S14 of Supporting Information S1).

We, therefore, find the hypothesis of enhanced TGM in the UTPC due to interhemispheric exchange to be congruent with CHC observations. We estimate that TGM in the UTPC most likely lags behind NH air mass intrusion flux by around 1 month, thus peaking around September. As for CHC, we attribute the strong TGM increase in 2015 to the significantly increased influence of westerly UT air masses, likely enriched in TGM due to UT interhemispheric exchange.

3.8. Reconstructed UTPC TGM Seasonality and a Comparison to CARIBIC Data

Following the hypothesis that TGM in the UTPC is driven by interhemispheric exchange, we developed a multilinear fit that explains 92% (95% CI: 84%–96%) of $dTGM/dt$ variation observed at CHC (Table S1 in Supporting Information S1). Our best fit suggests that UTPC TGM peaks around September, lagging behind UT NH to SH transport flux by about 1 month. The coefficients of this fit can be used to constrain the form of UTPC TGM seasonality even further: a ratio e/c_0 of 1.2 (Table S1 in Supporting Information S1) suggests that monthly UTPC TGM (c_U in Equation 2) varies within a year between c_0 and 2.2 c_0 (95% CI: $[1.6c_0, 3.4c_0]$), where c_0 is baseline TGM in the UTPC (corresponding to the month of May). In other words, we estimate that TGM in the UTPC is about twice as high in September as in May, the month of lowest TGM. Based on these results, we reconstructed the form of TGM seasonality in the UTPC, as shown in Figure 7a.

To validate this remotely reconstructed UTPC TGM seasonality, we compared it to in situ TGM measurements in the SH tropical UT, as provided by CARIBIC (see Section 2.7). Although no CARIBIC data is available for the SH Pacific, some data is provided further eastwards, for the eastern part of South America and the Atlantic Ocean. Considering the prevailing strong westerlies in the SH tropical UT (see Figure 5d), we can assume certain comparability between the seasonality of TGM in the UTPC and further eastward.

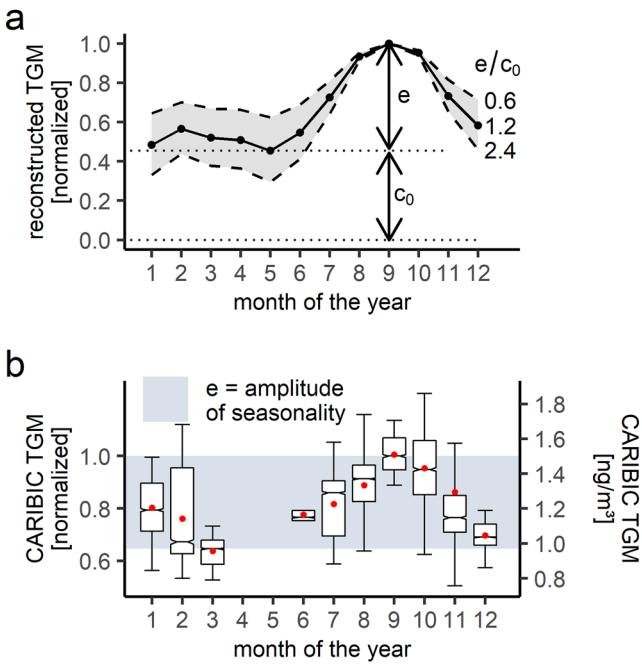


Figure 7. Reconstructed total gaseous mercury (TGM) seasonality and comparison to aircraft data on upper tropospheric TGM. (a) Reconstructed TGM seasonality in the upper tropospheric pacific channel (UTPC), based on Chacaltaya TGM under the hypothesis that UTPC TGM seasonality is driven by interhemispheric exchange. The magnitude of seasonality is expressed as ratio between amplitude of seasonal variation (e) and constant baseline concentration (c_0). Shaded area based on the 95% confidence interval of e/c_0 (0.6–2.4). (b) Measured upper tropospheric TGM seasonality east of the UTPC, based on CARIBIC flights between 2005 and 2016 (latitudes: 25°S–5°S, longitudes: −50° to −30°; for comparison, the UTPC was defined at ∼ −125°). Blue area: estimated amplitude of CARIBIC TGM seasonality, defined as difference between highest and lowest monthly median (September and March, respectively). Normalized values (left axis) obtained by division through the highest monthly median (September). Box plot outliers (<Q1 – 1.5 • IQR or > Q3 + 1.5 • IQR) are not shown. Red dots show mean values. Reconstructed (a) and measured (b) seasonality agree well, peaking simultaneously during September. While the amplitude of reconstructed seasonal variation appears higher than measured, the difference is not statistically significant ($\alpha = 0.05$), considering the e/c_0 95% confidence interval (shaded area in (a)).

We find that the reconstructed UTPC seasonality based on CHC TGM (Figure 7a) agrees well with the seasonality of CARIBIC TGM (Figure 7b) in the selected region of the SH tropics (longitude: −50° to −30°, latitude: 25°S–5°S). In both cases, TGM starts rising around June, peaks in September, and returns to baseline levels around December. Although the amplitude of seasonality is apparently larger for reconstructed TGM in the UTPC than for measured TGM further eastward, the difference is statistically not significant ($\alpha = 0.05$). We thus find that the UTPC TGM seasonality reconstructed from CHC TGM is congruent with CARIBIC TGM observations.

It is important to point out that following our approach CHC TGM is congruent with any TGM seasonality in the UTPC similar to the one presented in Figure 7, independently from its underlying driver. It is reassuring that the reconstructed seasonality agrees with CARIBIC TGM, but it is no conclusive evidence that this seasonality is in fact driven by interhemispheric exchange and not another process with a similar seasonal variation, like BB.

Nevertheless, we argue that BB unlikely drives such a large seasonal TGM variation: A recent modeling study estimated that BB increases UT CO in the region underlying our CARIBIC data selection, just east of South America, by around 10–20 ppbv between August and November (Cussac et al., 2020). Applying reported BB TGM/CO emission ratios, which are usually below 0.002 ng/m^3 (Ebinghaus et al., 2007; Koenig et al., 2021; Wang et al., 2015), to such CO enhancements in a back-of-the-envelope calculation yields an "explained" TGM enhancement of just ∼0.04 ng/m^3. This is ∼10 times lower than the magnitude of UT TGM seasonality shown here (Figure 7). It must be said that the atmospheric lifetime of CO is around 1–2 months (Khalil & Rasmussen, 1990), considerably shorter than the atmospheric lifetime of Hg (5.2 months–1.7 yr, see introduction). Consequently, the TGM/CO ratio grows with increasing traveling time from wildfires (McLagan et al., 2021). While this would impact the above estimate, we note that reported BB TGM/CO emission ratios were often obtained far from wildfires, such that the difference in atmospheric lifetimes of CO and TGM is to some degree already included in these estimates (McLagan et al., 2021).

Considering all this, we believe that interhemispheric exchange is the main driver of TGM seasonality in the SH tropical UT, exceeding BB. Either way, given their similar seasonality, the two drivers most likely overlap and reinforce each other.

4. Conclusions and Outlook

We explored plausible causes for the strong Hg increase at CHC in 2015. We discussed, based on published literature, transport modeling and some available ancillary data, the potential role of changes in BB emissions in tropical South America, vegetation Hg uptake of the Amazon rainforest, and oceanic surface Hg emissions from the equatorial or SH tropical Pacific. While the exact influence of these factors has not been formally quantified here, we consider them to be possible contributing elements but unlikely main drivers of the observed Hg increase.

Instead, we found that this strong Hg increase could be explained by the intensification of a westerly UT transport pathway over the SH tropical Pacific, carrying strongly NH influenced air masses to South America. We estimate that interhemispheric exchange drives Hg seasonality in the SH tropical Pacific UT, leading to elevated Hg between July and October. We found such a seasonality to be in line with in situ aircraft data on atmospheric Hg in the SH tropical UT.

Nevertheless, we highlight the need for more continuous Hg measurements in tropical south America to confirm these results, which are limited by the relatively short TGM time series at CHC and were obtained through a series of simplifications, such as the non-consideration of chemical transformations during transport. We also highlight the need for more aircraft Hg data, preferentially over the tropical Pacific and the tropical Indian Ocean, to better understand and quantify interhemispheric Hg exchange as a large and seasonally variable Hg input into the SH.

We suggest, regarding the strong Hg rise at CHC in 2015, to view the 2015–2016 El Niño as a "natural experiment": in 2015, CHC air mass origin shifted steadily west- and vertically upwards (Figure 3b), offering a closer look into preferential pathways of interhemispheric Hg exchange over the tropical Pacific and likely the tropical Indian Ocean. It should be noted that no important ENSO-related anomaly in the magnitude of interhemispheric exchange was necessary to explain the CHC Hg increase (Figure 5c), and we draw no conclusions on the impact of ENSO on interhemispheric air mass exchange as a whole. Moreover, all obtained model fits are valid for both the 2015–2016 El Niño and the ENSO-neutral year before (Figures 4 and 6). Thus, by enhancing transport to CHC through the tropical Pacific UT, the 2015–2016 El Niño might have only opened a window that allowed us to look more closely at a regular aspect of interhemispheric Hg exchange. We propose that this "natural experiment" offered by El Niño, and CHC Hg observations, could be used as a reference to test the representation of interhemispheric transport in Hg models, and to constrain Hg tropospheric lifetime as well as Hg emission and re-emission fluxes.

Data Availability Statement

Chacaltaya L1 TGM data (https://doi.org/10.25326/347) are freely available (Magand & Dommergue, 2022) at https://gmos.aeris-data.fr/ from a GMOS-FR data portal coordinated by IGE (Institut des Géosciences de l'Environnement—Grenoble, France; technical PI: Olivier Magand) with the support of the French national AERIS-SEDOO partners, data and services center for the atmosphere (last access: 11 September 2021). Chacaltaya aethalometer data on equivalent BC is freely available under https://www.gaw-wdca.org/Browse-Obtain-Data (last access: 10 September 2021). Data on the ENSO indices ONI, SOI, and MEI are freely available from NOAA, under https://psl.noaa.gov/enso/dashboard.html (last access: 10 September 2021). Chacaltaya carbon monoxide data will be made available upon acceptance at Velarde (2022, https://doi.org/10.5061/dryad.kd51c5b7x). CARIBIC data is available upon request from IAGOS under https://www.caribic-atmospheric.com/Data.php (last access: 10 September 2021).

Acknowledgments
The authors acknowledge the contribution of Ralf Ebinghaus to CARIBIC data. The authors thank Jennie Thomas and Diego Aliaga for scientific discussions and constructive comments on the manuscript. Financial support was granted through fundings from Institut Universitaire de France, LabEX OSUG@2020, LEFE CNRS/INSU, SNO CLAP as well as by ACTRIS-France National Research infrastructure. The authors thank IRD (Institut de Recherche pour le Développement) and LFA for their logistical support during the field campaign. CHC TGM data were collected via instruments coordinated by the IGE-PTICHA technical platform dedicated to atmospheric chemistry field instrumentation. The L1 Chacaltaya GMOS–Fr database is maintained by the French national center for Atmospheric data and services AERIS. This study was supported by the UMSA (Universidad Mayor de San Andrés) through the Laboratory for Atmospheric Physics (LFA) of the Institute for Physics Research. The LFA provided scientific, administrative, and logistical support. IAGOS-CARIBIC data were created with support from the European Commission, national agencies in Germany (BMBF), France (MESR), and the UK (NERC), and the IAGOS member institutions (http://www.iagos.org/partners). This publication is part of the GMOS-Train project that has received funding from the European Union's Horizon 2020 research and innovation program under the Marie Skłodowska-Curie grant agreement No. 860497.

References

Aghedo, A. M., Rast, S., & Schultz, M. G. (2010). Sensitivity of tracer transport to model resolution, prescribed meteorology, and tracer lifetime in the general circulation model ECHAM5. *Atmospheric Chemistry and Physics*, *10*(7), 3385–3396. https://doi.org/10.5194/acp-10-3385-2010

Aliaga, D., Sinclair, V. A., Andrade, M., Artaxo, P., Carbone, S., Kadantsev, E., et al. (2021). Identifying source regions of air masses sampled at the tropical high-altitude site of Chacaltaya using WRF-FLEXPART and cluster analysis. *Atmospheric Chemistry and Physics*, *21*(21), 16453–16477. https://doi.org/10.5194/acp-21-16453-2021

Ambrizzi, T., de Souza, E. B., & Pulwarty, R. S. (2004). The Hadley and Walker regional circulations and associated ENSO impacts on South American seasonal rainfall. In H. F. Diaz & R. S. Bradley (Eds.), *The Hadley circulation: Present, past, and future* (Vol. 21, pp. 203–235). Springer Netherlands. https://doi.org/10.1007/978-1-4020-2944-8_8

Andrade, M., Zaratti, F., Forno, R., Gutiérrez, R., Moreno, I., Velarde, F., et al. (2015). Puesta en marcha de una nueva estación de monitoreo climático en los andes centrales de Bolivia: La estación Gaw/Chacaltaya. *Revista Boliviana de Física*, *26*, 6–15.

Ariya, P. A., Amyot, M., Dastoor, A., Deeds, D., Feinberg, A., Kos, G., et al. (2015). Mercury physicochemical and biogeochemical transformation in the atmosphere and at atmospheric interfaces: A review and future directions. *Chemical Reviews*, *115*(10), 3760–3802. https://doi.org/10.1021/cr500667e

Bastos, A., Friedlingstein, P., Sitch, S., Chen, C., Mialon, A., Wigneron, J.-P., et al. (2018). Impact of the 2015/2016 El Niño on the terrestrial carbon cycle constrained by bottom-up and top-down approaches. *Philosophical Transactions of the Royal Society B: Biological Sciences*, *373*(1760), 20170304. https://doi.org/10.1098/rstb.2017.0304

Berghaus, D. G., & Cannon, J. P. (1973). Obtaining derivatives from experimental data using smoothed-spline functions: The smoothed cubic spline is presented for use in obtaining high-quality derivatives from experimental data and example applications are shown for scattered-light photoelasticity and the bending of beams. *Experimental Mechanics*, *13*(1), 38–42. https://doi.org/10.1007/BF02319311

Bianchi, F., Sinclair, V. A., Aliaga, D., Zha, Q., Scholz, W., Wu, C., et al. (2022). The SALTENA experiment: Comprehensive observations of aerosol sources, formation, and processes in the South American Andes. *Bulletin of the American Meteorological Society*, *103*(2), E212–E229. https://doi.org/10.1175/BAMS-D-20-0187.1

Bowman, K. P., & Cohen, P. J. (1997). Interhemispheric exchange by seasonal modulation of the Hadley circulation. *Journal of the Atmospheric Sciences*, *54*(16), 2045–2059. https://doi.org/10.1175/1520-0469(1997)054<2045:IEBSMO>2.0.CO;2

Chatterjee, A., Gierach, M. M., Sutton, A. J., Feely, R. A., Crisp, D., Eldering, A., et al. (2017). Influence of El Niño on atmospheric CO_2 over the tropical Pacific Ocean: Findings from NASA's OCO-2 mission. *Science*, *358*(6360), eaam5776. https://doi.org/10.1126/science.aam5776

Chauvigné, A., Aliaga, D., Sellegri, K., Montoux, N., Krejci, R., Močnik, G., et al. (2019). Biomass burning and urban emission impacts in the Andes Cordillera region based on in situ measurements from the Chacaltaya Observatory, Bolivia (5,240 m asl). *Atmospheric Chemistry and Physics*, *19*(23), 14805–14824. https://doi.org/10.5194/acp-19-14805-2019

Chen, G., Orbe, C., & Waugh, D. (2017). The role of monsoon-like zonally asymmetric heating in interhemispheric transport: Monsoon and interhemispheric transport. *Journal of Geophysical Research: Atmospheres*, *122*(6), 3282–3298. https://doi.org/10.1002/2016JD026427

Chen, Y., Randerson, J. T., Morton, D. C., DeFries, R. S., Collatz, G. J., Kasibhatla, P. S., et al. (2011). Forecasting fire season severity in South America using sea surface temperature anomalies. *Science*, *334*(6057), 787–791. https://doi.org/10.1126/science.1209472

Cussac, M., Marécal, V., Thouret, V., Josse, B., & Sauvage, B. (2020). The impact of biomass burning on upper tropospheric carbon monoxide: A study using MOCAGE global model and IAGOS airborne data. *Atmospheric Chemistry and Physics*, *20*(15), 9393–9417. https://doi.org/10.5194/acp-20-9393-2020

Czeplak, G., & Junge, C. (1975). Studies of interhemispheric exchange in the troposphere by a diffusion model. In *Advances in geophysics* (Vol. 18, pp. 57–72). Elsevier. https://doi.org/10.1016/S0065-2687(08)60571-3

D'Amore, F., Bencardino, M., Cinnirella, S., Sprovieri, F., & Pirrone, N. (2015). Data quality through a web-based QA/QC system: Implementation for atmospheric mercury data from the global mercury observation system. *Environmental Science: Processes & Impacts*, *17*(8), 1482–1491. https://doi.org/10.1039/C5EM00205B

Eastham, S. D., & Jacob, D. J. (2017). Limits on the ability of global Eulerian models to resolve intercontinental transport of chemical plumes. *Atmospheric Chemistry and Physics*, *17*(4), 2543–2553. https://doi.org/10.5194/acp-17-2543-2017

Ebinghaus, R., Slemr, F., Brenninkmeijer, C. A. M., van Velthoven, P., Zahn, A., Hermann, M., et al. (2007). Emissions of gaseous mercury from biomass burning in South America in 2005 observed during CARIBIC flights: HG emission from biomass burning. *Geophysical Research Letters*, *34*(8). https://doi.org/10.1029/2006GL028866

Francey, R. J., & Frederiksen, J. S. (2016). The 2009–2010 step in atmospheric CO_2 interhemispheric difference. *Biogeosciences*, *13*(3), 873–885. https://doi.org/10.5194/bg-13-873-2016

Frederiksen, J. S., & Francey, R. J. (2018). Unprecedented strength of Hadley circulation in 2015–2016 impacts on CO_2 interhemispheric difference. *Atmospheric Chemistry and Physics*, *18*(20), 14837–14850. https://doi.org/10.5194/acp-18-14837-2018

Geller, L. S., Elkins, J. W., Lobert, J. M., Clarke, A. D., Hurst, D. F., Butler, J. H., & Myers, R. C. (1997). Tropospheric SF_6: Observed latitudinal distribution and trends, derived emissions, and interhemispheric exchange time. *Geophysical Research Letters*, *24*(6), 675–678. https://doi.org/10.1029/97GL00523

Gerson, J. R., Szponar, N., Zambrano, A. A., Bergquist, B., Broadbent, E., Driscoll, C. T., et al. (2022). Amazon forests capture high levels of atmospheric mercury pollution from artisanal gold mining. *Nature Communications*, *13*(1), 559. https://doi.org/10.1038/s41467-022-27997-3

Gonzalez-Raymat, H., Liu, G., Liriano, C., Li, Y., Yin, Y., Shi, J., et al. (2017). Elemental mercury: Its unique properties affect its behavior and fate in the environment. *Environmental Pollution*, *229*, 69–86. https://doi.org/10.1016/j.envpol.2017.04.101

Gratz, L. E., Ambrose, J. L., Jaffe, D. A., Shah, V., Jaeglé, L., Stutz, J., et al. (2015). Oxidation of mercury by bromine in the subtropical Pacific free troposphere. *Geophysical Research Letters*, *42*(23). https://doi.org/10.1002/2015GL066645

Grimm, A. M., & Ambrizzi, T. (2009). Teleconnections into South America from the tropics and extratropics on interannual and intraseasonal timescales. In *Past climate variability in South America and surrounding regions* (pp. 159–191). Dordrecht: Springer. https://doi.org/10.1007/978-90-481-2672-9_7

Guédron, S., Point, D., Acha, D., Bouchet, S., Baya, P. A., Tessier, E., et al. (2017). Mercury contamination level and speciation inventory in Lakes Titicaca & Uru-Uru (Bolivia): Current status and future trends. *Environmental Pollution*, *231*, 262–270. https://doi.org/10.1016/j.envpol.2017.08.009

Gustin, M. S., Dunham-Cheatham, S. M., Zhang, L., Lyman, S., Choma, N., & Castro, M. (2021). Use of membranes and detailed HYSPLIT analyses to understand atmospheric particulate, gaseous oxidized, and reactive mercury chemistry. *Environmental Science & Technology*, *55*(2), 893–901. https://doi.org/10.1021/acs.est.0c07876

Horowitz, H. M., Jacob, D. J., Zhang, Y., Dibble, T. S., Slemr, F., Amos, H. M., et al. (2017). A new mechanism for atmospheric mercury redox chemistry: Implications for the global mercury budget. *Atmospheric Chemistry and Physics*, *17*(10), 6353–6371. https://doi.org/10.5194/acp-17-6353-2017

Howard, D., Nelson, P. F., Edwards, G. C., Morrison, A. L., Fisher, J. A., Ward, J., et al. (2017). Atmospheric mercury in the Southern Hemisphere tropics: Seasonal and diurnal variations and influence of inter-hemispheric transport. *Atmospheric Chemistry and Physics*, *17*(18), 11623–11636. https://doi.org/10.5194/acp-17-11623-2017

Huang, S., & Zhang, Y. (2021). Interannual variability of air-sea exchange of mercury in the global ocean: The "seesaw effect" in the equatorial Pacific and contributions to the atmosphere. *Environmental Science & Technology*, *55*(10), 7145–7156. https://doi.org/10.1021/acs.est.1c00691

Jaffe, D., Prestbo, E., Swartzendruber, P., Weisspenzias, P., Kato, S., Takami, A., et al. (2005). Export of atmospheric mercury from Asia. *Atmospheric Environment*, *39*(17), 3029–3038. https://doi.org/10.1016/j.atmosenv.2005.01.030

Jiskra, M., Sonke, J. E., Obrist, D., Bieser, J., Ebinghaus, R., Myhre, C. L., et al. (2018). A vegetation control on seasonal variations in global atmospheric mercury concentrations. *Nature Geoscience*, *11*(4), 244–250. https://doi.org/10.1038/s41561-018-0078-8

Khalil, M. A. K., & Rasmussen, R. A. (1990). The global cycle of carbon monoxide: Trends and mass balance. *Chemosphere*, *20*(1–2), 227–242. https://doi.org/10.1016/0045-6535(90)90098-E

Koenig, A. M., Magand, O., Laj, P., Andrade, M., Moreno, I., Velarde, F., et al. (2021). Seasonal patterns of atmospheric mercury in tropical South America as inferred by a continuous total gaseous mercury record at Chacaltaya station (5,240 m) in Bolivia. *Atmospheric Chemistry and Physics*, *21*(5), 3447–3472. https://doi.org/10.5194/acp-21-3447-2021

Koren, G., van Schaik, E., Araújo, A. C., Boersma, K. F., Gärtner, A., Killaars, L., et al. (2018). Widespread reduction in sun-induced fluorescence from the Amazon during the 2015/2016 El Niño. *Philosophical Transactions of the Royal Society B: Biological Sciences*, *373*(1760), 20170408. https://doi.org/10.1098/rstb.2017.0408

Lamborg, C. H., Fitzgerald, W. F., O'Donnell, J., & Torgersen, T. (2002). A non-steady-state compartmental model of global-scale mercury biogeochemistry with interhemispheric atmospheric gradients. *Geochimica et Cosmochimica Acta*, *66*(7), 1105–1118. https://doi.org/10.1016/S0016-7037(01)00841-9

Lau, K.-M., & Yang, S. (2015). Tropical meteorology & climatelWalker circulation. In *Encyclopedia of atmospheric sciences* (pp. 177–181). Elsevier. https://doi.org/10.1016/B978-0-12-382225-3.00450-3

Li, C., Sonke, J. E., Le Roux, G., Piotrowska, N., Van der Putten, N., Roberts, S. J., et al. (2020). Unequal anthropogenic enrichment of mercury in Earth's Northern and Southern Hemispheres. *ACS Earth and Space Chemistry*, *4*(11), 2073–2081. https://doi.org/10.1021/acsearthspacechem.0c00220

Li, Y., Li, J., Jin, F. F., & Zhao, S. (2015). Interhemispheric propagation of stationary Rossby waves in a horizontally nonuniform background flow. *Journal of the Atmospheric Sciences*, *72*(8), 3233–3256. https://doi.org/10.1175/JAS-D-14-0239.1

Liu, J., Bowman, K. W., Schimel, D. S., Parazoo, N. C., Jiang, Z., Lee, M., et al. (2017). Contrasting carbon cycle responses of the tropical continents to the 2015–2016 El Niño. *Science*, *358*(6360), eaam5690. https://doi.org/10.1126/science.aam5690

Magand, O., & Dommergue, A. (2022). Continuous measurements of atmospheric mercury at Chacaltaya Observatory (L1) [Data set] [CSV]. Aeris. https://doi.org/10.25326/347

McLagan, D. S., Stupple, G. W., Darlington, A., Hayden, K., & Steffen, A. (2021). Where there is smoke there is mercury: Assessing boreal forest fire mercury emissions using aircraft and highlighting uncertainties associated with upscaling emissions estimates. *Atmospheric Chemistry and Physics*, *21*(7), 5635–5653. https://doi.org/10.5194/acp-21-5635-2021

Miyazaki, K., Machida, T., Patra, P. K., Iwasaki, T., Sawa, Y., Matsueda, H., & Nakazawa, T. (2009). Formation mechanisms of latitudinal CO_2 gradients in the upper troposphere over the subtropics and tropics. *Journal of Geophysical Research*, *114*(D3), D03306. https://doi.org/10.1029/2008JD010545

Munthe, J., Sprovieri, F., Horvat, M., & Ebinghaus, R. (2011). *R.: SOPs and QA/QC protocols regarding measurements of TGM, GEM, RGM, TPM, and mercury in precipitation in cooperation with WP3, WP4, and WP5. GMOS deliverable 6.1, CNR-IIA, IVL.* Retrieved from http://www.gmos.eu

Newell, R. E., Vincent, D. G., & Kidson, J. W. (1969). Interhemispheric mass exchange from meteorological and trace substance observations. *Tellus*, *21*(5), 641–647. https://doi.org/10.3402/tellusa.v21i5.10114

Obrist, D., Kirk, J. L., Zhang, L., Sunderland, E. M., Jiskra, M., & Selin, N. E. (2018). A review of global environmental mercury processes in response to human and natural perturbations: Changes of emissions, climate, and land use. *Ambio*, *47*(2), 116–140. https://doi.org/10.1007/s13280-017-1004-9

Orbe, C., Waugh, D. W., Newman, P. A., & Steenrod, S. (2016). The transit-time distribution from the Northern Hemisphere midlatitude surface. *Journal of the Atmospheric Sciences*, *73*(10), 3785–3802. https://doi.org/10.1175/JAS-D-15-0289.1

Patra, P. K., Takigawa, M., Dutton, G. S., Uhse, K., Ishijima, K., Lintner, B. R., et al. (2009). Transport mechanisms for synoptic, seasonal, and interannual SF_6 variations and "age" of air in troposphere. *Atmospheric Chemistry and Physics*, *9*(4), 1209–1225. https://doi.org/10.5194/acp-9-1209-2009

Prather, M., McElroy, M., Wofsy, S., Russell, G., & Rind, D. (1987). Chemistry of the global troposphere: Fluorocarbons as tracers of air motion. *Journal of Geophysical Research*, *92*(D6), 6579. https://doi.org/10.1029/JD092iD06p06579

Riddle, E. E., Voss, P. B., Stohl, A., Holcomb, D., Maczka, D., Washburn, K., & Talbot, R. W. (2006). Trajectory model validation using newly developed altitude-controlled balloons during the International Consortium for atmospheric research on transport and transformations 2004 campaign: Balloon validation of trajectory models. *Journal of Geophysical Research: Atmospheres*, *111*(D23). https://doi.org/10.1029/2006JD007456

Saiz-Lopez, A., Sitkiewicz, S. P., Roca-Sanjuán, D., Oliva-Enrich, J. M., Dávalos, J. Z., Notario, R., et al. (2018). Photoreduction of gaseous oxidized mercury changes global atmospheric mercury speciation, transport, and deposition. *Nature Communications*, *9*(1), 4796. https://doi.org/10.1038/s41467-018-07075-3

Saiz-Lopez, A., Travnikov, O., Sonke, J. E., Thackray, C. P., Jacob, D. J., Carmona-García, J., et al. (2020). Photochemistry of oxidized Hg(I) and Hg(II) species suggests missing mercury oxidation in the troposphere. *Proceedings of the National Academy of Sciences*, *117*(49), 30949–30956. https://doi.org/10.1073/pnas.1922486117

Schneider, T., Bischoff, T., & Haug, G. H. (2014). Migrations and dynamics of the intertropical convergence zone. *Nature*, *513*(7516), 45–53. https://doi.org/10.1038/nature13636

Schroeder, W. H., & Munthe, J. (1998). Atmospheric mercury—An overview. *Atmospheric Environment*, *32*(5), 809–822. https://doi.org/10.1016/S1352-2310(97)00293-8

Selin, N. E., Jacob, D. J., Park, R. J., Yantosca, R. M., Strode, S., Jaeglé, L., & Jaffe, D. (2007). Chemical cycling and deposition of atmospheric mercury: Global constraints from observations. *Journal of Geophysical Research*, *112*(D2), D02308. https://doi.org/10.1029/2006JD007450

Shah, V., Jacob, D. J., Thackray, C. P., Wang, X., Sunderland, E. M., Dibble, T. S., et al. (2021). Improved mechanistic model of the atmospheric redox chemistry of mercury. *Environmental Science & Technology*, *55*(21), 14445–14456. https://doi.org/10.1021/acs.est.1c03160

Slemr, F., Brenninkmeijer, C. A., Rauthe-Schöch, A., Weigelt, A., Ebinghaus, R., Brunke, E.-G., et al. (2016). El Niño-Southern Oscillation influence on tropospheric mercury concentrations. *Geophysical Research Letters*, *43*(4), 1766–1771. https://doi.org/10.1002/2016GL067949

Slemr, F., Ebinghaus, R., Brenninkmeijer, C. A. M., Hermann, M., Kock, H. H., Martinsson, B. G., et al. (2009). Gaseous mercury distribution in the upper troposphere and lower stratosphere observed onboard the CARIBIC passenger aircraft. *Atmospheric Chemistry and Physics*, *9*(6), 1957–1969. https://doi.org/10.5194/acp-9-1957-2009

Song, S., Selin, N. E., Soerensen, A. L., Angot, H., Artz, R., Brooks, S., et al. (2015). Top-down constraints on atmospheric mercury emissions and implications for global biogeochemical cycling. *Atmospheric Chemistry and Physics*, *15*(12), 7103–7125. https://doi.org/10.5194/acp-15-7103-2015

Sprovieri, F., Pirrone, N., Bencardino, M., D'Amore, F., Carbone, F., Cinnirella, S., et al. (2016). Atmospheric mercury concentrations observed at ground-based monitoring sites globally distributed in the framework of the GMOS network. *Atmospheric Chemistry and Physics*, *16*(18), 11915–11935. https://doi.org/10.5194/acp-16-11915-2016

Stein, A. F., Draxler, R. R., Rolph, G. D., Stunder, B. J. B., Cohen, M. D., & Ngan, F. (2015). NOAA's HYSPLIT atmospheric transport and dispersion modeling system. *Bulletin of the American Meteorological Society*, *96*(12), 2059–2077. https://doi.org/10.1175/BAMS-D-14-00110.1

Streets, D. G., Horowitz, H. M., Jacob, D. J., Lu, Z., Levin, L., ter Schure, A. F. H., & Sunderland, E. M. (2017). Total mercury released to the environment by human activities. *Environmental Science & Technology*, *51*(11), 5969–5977. https://doi.org/10.1021/acs.est.7b00451

Strode, S. A., Jaeglé, L., Jaffe, D. A., Swartzendruber, P. C., Selin, N. E., Holmes, C., & Yantosca, R. M. (2008). Trans-Pacific transport of mercury. *Journal of Geophysical Research*, *113*(D15), D15305. https://doi.org/10.1029/2007JD009428

Travnikov, O., Angot, H., Artaxo, P., Bencardino, M., Bieser, J., D'Amore, F., et al. (2017). Multi-model study of mercury dispersion in the atmosphere: Atmospheric processes and model evaluation. *Atmospheric Chemistry and Physics*, *17*(8), 5271–5295. https://doi.org/10.5194/acp-17-5271-2017

UN-Environment. (2019). *Global Mercury Assessment 2018*. Geneva, Switzerland: UN Environment Programme, Chemicals and Health Branch. Retrieved from https://www.amap.no/documents/doc/global-mercury-assessment-2018/1757

Velarde, F. (2022). carbon_monoxide_gaw_chacaltaya [Data set]. Submitted by Fernando Velarde. https://doi.org/10.5061/dryad.kd51c5b7x

Wang, X., Zhang, H., Lin, C., Fu, X., Zhang, Y., & Feng, X. (2015). Transboundary transport and deposition of Hg emission from springtime biomass burning in the Indo-China Peninsula. *Journal of Geophysical Research: Atmospheres*, *120*(18), 9758–9771. https://doi.org/10.1002/2015JD023525

Yan, X., Konopka, P., Hauck, M., Podglajen, A., & Ploeger, F. (2021). Asymmetry and pathways of inter-hemispheric transport in the upper troposphere and lower stratosphere. *Atmospheric Chemistry and Physics*, *21*(9), 6627–6645. https://doi.org/10.5194/acp-21-6627-2021

Yu, K., Keller, C. A., Jacob, D. J., Molod, A. M., Eastham, S. D., & Long, M. S. (2018). Errors and improvements in the use of archived meteorological data for chemical transport modeling: An analysis using GEOS-Chem v11-01 driven by GEOS-5 meteorology. *Geoscientific Model Development*, *11*(1), 305–319. https://doi.org/10.5194/gmd-11-305-2018

Zhou, J., Obrist, D., Dastoor, A., Jiskra, M., & Ryjkov, A. (2021). Vegetation uptake of mercury and impacts on global cycling. *Nature Reviews Earth & Environment*, *2*(4), 269–284. https://doi.org/10.1038/s43017-021-00146-y

Zhuang, J., Jacob, D. J., & Eastham, S. D. (2018). The importance of vertical resolution in the free troposphere for modeling intercontinental plumes. *Atmospheric Chemistry and Physics*, *18*(8), 6039–6055. https://doi.org/10.5194/acp-18-6039-2018